POLITECNICO DI MILANO

Scuola di Ingegneria Industriale e dell'Informazione
Corso di Laurea Magistrale in Ingegneria Aeronautica

Immersed boundary simulation of turbulent flow through a peristaltic actuator

Relatore:
Prof. Maurizio Quadrio

Tesi di Laurea Magistrale di:
Francesco Secchi
Matr. 863463

Anno Accademico 2017-2018

Contents

List of Figures

List of Tables

Abstract

In this study a numerical code for the simulation of turbulent channel flows with non-planar moving walls is presented. The solid boundaries of the channel are immersed within the frame of a fixed non-body-conformal Cartesian grid. Spatial discretization of the incompressible Navier-Stokes equations (in primitive variables) is performed using second-order accurate finite differences. A three-step Runge-Kutta method is applied in conjunction with a fractional step technique for time advancement. The key novelty of the numerical technique lies in an innovative implementation of the Immersed Boundary Method (IBM). No-slip boundary conditions on immersed solid walls are enforced through an interpolation-free procedure applied to the discrete momentum equation.

The ability of the flow solver to resolve a complex turbulent channel flow in the presence of moving walls is tested by simulating a peristaltic actuator for turbulent skin-friction drag reduction. In accordance with existing results, a downstream traveling peristaltic wave of wall deformation is proved to allow for large drag reduction rates. Further, under some sets of parameters, a full relaminarization of the flow is observed.

Keywords— Immersed Boundary Method, Turbulence, Flow control, Skin-friction drag reduction, Peristalsis

Sommario

Nel presente studio viene presentato un codice numerico per la simulazione di correnti turbolente attraverso canali confinati da pareti non piane e dotate di movimento. I contorni solidi del canale sono immersi in una griglia cartesiana che rimane fissa durante la simulazione. La discretizzazione spaziale delle equazioni incomprimibili di Navier-Stokes (in variabili primitive) viene eseguita attraverso differenze finite del secondo ordine. Uno schema Runge-Kutta a tre passi è utilizzato insieme ad uno schema di tipo fractional step per l'avanzamento temporale delle equazioni discrete. L'elemento di innovazione del seguente codice è rappresentato da una particolare implementazione del metodo dei contorni immersi. Le condizioni di adesione sui contorni solidi del dominio sono imposte attraverso l'aggiunta di un termine correttivo all'equazione della quantità di moto in forma discreta. La procedura risulta relativamente semplice in quanto non richiede alcuna forma di interpolazione.
L'efficacia del metodo numerico è testata simulando il funzionamento di un attuatore peristaltico per la riduzione di resistenza d'attrito turbolenta. In accordo con risultati già presenti in letteratura, viene dimostrata l'efficacia di questo dispositivo nel promuovere la riduzione di resistenza. Inoltre, per alcuni gruppi di parametri di attuazione, si osserva una completa rilaminarizzazione della corrente.

Parole chiave— Metodo dei contorni immersi, Turbolenza, Flow control, Riduzione di resistenza turbolenta, Peristalsi

Chapter 1

Introduction

A great span of real-world applications has to face with fluid flows that are almost always turbulent. Wall-bounded turbulent flows are characterized by a large skin-friction drag caused by the near-wall coherent structures which are responsible for turbulent production. Consequently, turbulence has a significant impact on the power spent for vehicle's locomotion and for pumping liquids through pipelines. Considerable savings, in terms of fuel costs and environmental impact, could be attained if an effective strategy were developed to take advantage of fluid-dynamics and reduce the skin-friction drag. During recent years great efforts have been spent in this direction: passive flow control strategies (such as riblets) have been intensively investigated and proved to lead up to $7\% - 8\%$ drag reduction rates ([51]), while active control strategies showed even better performances in weakening turbulence and allowing for large drag reduction rates. Among the numerous active control techniques, those involving pre-determined traveling waves are very attractive because of their simplicity and efficacy ([31], [30], [35]).

Direct numerical simulations (DNS) have been the primary tool for the investigation and the development of new flow control techniques in wall-bounded turbulent flows. However, the computational cost required is extremely high, limiting the applicability of DNS only to low Reynolds number flows. Hence, parallel to the development of new flow control strategies, there's the interest in designing and implementing efficient computational flow solvers. On this respect immersed boundary methods (IBM) are attractive as they allow for accurate flow simulations in the presence of complex solid boundaries (either stationary or moving) and retain a relatively low computational cost ([32], [18]).

The present study aims at adapting an already existing IBM flow solver (developed by Paolo Luchini) for the simulation of turbulent channel flows with non-planar moving walls. Further, an application to the active flow control method of streamwise traveling waves of wall deformation (peristalsis) is presented.

After this brief introductory section, the work is organized as follows:

- Chapter 2 furnishes a short introduction to the nature of turbulent flows and the standard approaches to the study of the subject;

- Chapter 3 reviews motivations and approaches to the theme of turbulent flow control for skin-friction drag reduction. Further, control strategies involving streamwise waves of actuation are presented in some detail;

- Chapter 4 is intended to give a detailed description of the immersed-boundary flow solver. First, a general overview is given, starting from the governing equations and their spatial and temporal discretization. Later, the treatment of solid immersed boundaries is presented. In the final part of the chapter some aspects on the structure of the numerical code, along with measured parallel scaling performances, are presented;

- Chapter 5 presents the application of the numerical method to the flow control strategy of streamwise traveling waves of wall deformation. First, the setup of the numerical experiments is reported. Then, some details about the averaging techniques used to ascertain statistical flow quantities are discussed. Later, the results obtained from the simulations are presented; initially flow characteristics are explained, then drag reduction effects are discussed;

- Chapter 6 reports the concluding remarks of the work and discusses some possible future developments.

Chapter 2

General background

2.1 Turbulent flows

It could be argued that turbulent flows represent the most important fluid flows encountered in the physical world. Turbulence is indeed fundamental for explaining many different natural phenomena and it is largely exploited by a great variety of engineering applications. Even though turbulent flows surround our everyday's life, a precise and accepted definition of turbulence still lacks. Nevertheless, it is commonly agreed to refer to turbulent flow as a fluid motion displaying certain peculiar characteristics. Namely, it could be stated that all turbulent flows are, in some way, chaotic, unpredictable and random. In fig.2.1 it is represented the turbulent wake behind a bullet traveling at a subsonic speed in still air. It can be noticed the high complexity of the flow-field: apparently many different scales are involved contemporarily in the fluid motion. Large structures, comparable to the wake width, down to small eddies, almost indistinguishable to the picture resolution, are readily recognized in the figure.

Further, another feature of great importance is that turbulent flows enhance significantly transfer and mixing of heat, mass and momentum. While at times this comes as an advantage that can be exploited to favor mixing of chemical reactants or enhance heat transfer, at other times the same feature should be reduced as much as possible to overcome, for example, the large wall shear stress exhibited by wall-bounded turbulent flows. On this respect, it should be also emphasized that turbulence is an extremely dissipative phenomenon and, as such, it requires energy to survive.

The origin of turbulence as a well-established branch of fluid dynamics may be traced back to the pioneering work of Osborne Reynolds [42], who recognized the important competing roles of fluid inertia and viscosity in promoting flow transition from laminar to turbulent. He established that the flow behavior could be characterized by the value of a simple non-

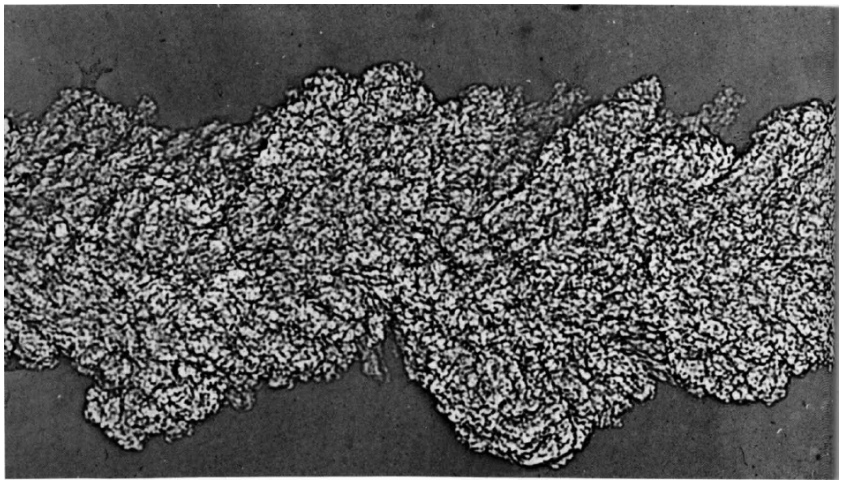

Figure 2.1: *Turbulent wake behind a bullet traveling at subsonic speed in still air. From [6]*

dimensional parameter, called Reynolds number, defined as:

$$Re = \frac{U\,L}{\nu} \tag{2.1}$$

where U and L are, respectively, appropriate reference velocity and length scales of the geometry and ν is the kinematic viscosity of the fluid. It can be stated that the Reynolds number represents a sensitivity parameter of the flow with respect to the propagation and amplification of disturbances [39]. Broadly speaking, the larger the Reynolds number, the more the flow is likely to develop instabilities that can quickly bring it to a fully developed turbulent state. Importantly, the vast majority of fluid flows of practical interest is characterized by very large Reynolds numbers; hence one may be led to the conclusion that, in fluid dynamics, laminar flow is the exception, not the rule [14]. Only in particular circumstances length scales are so small and viscous effects are so significant that it is likely to encounter a stable laminar flow (for instance, a notable exception is microfluidic).

Along with this relevant, yet practical, matter, research on turbulence is also motivated by the intriguing nature of the subject. A representative, often quoted, caption on this respect is due to R. Feynman, who asserted that "turbulence is the most important unsolved problem of classical physics". Even though turbulence research has made a great stride forward, the feeling concealed in Feynman's assertion is still considered valid by many authors [5].

A brief review of the classical approaches to the analysis of turbulent flows is presented in the following section.

2.2 Method of analysis

Governing equations

Turbulent flows, as well as laminar flows, are governed by the well-known Navier-Stokes equations. The present work is concerned only with incompressible flows and, in this case, the equations of motion read:

$$\frac{\partial \mathbf{u}}{\partial t} + (\mathbf{u} \cdot \nabla)\,\mathbf{u} = -\nabla p + \nu \nabla^2 \mathbf{u} \tag{2.2a}$$

$$\nabla \cdot \mathbf{u} = 0 \tag{2.2b}$$

where $\mathbf{u}$ represents the velocity, p is the pressure (divided by the fluid density) and ν is the kinematic viscosity of the fluid. Eq.2.2a simply states Newton's second law applied to a fluid element, while eq.2.2b represents the incompressibility constraint. It is known that pressure appears inside the governing equations 2.2 simply as a Lagrange multiplier needed to enforce the incompressibility constraint eq.2.2b. Thus, in these circumstances, the Navier-Stokes equations 2.2, along with proper initial and boundary conditions, represent a closed system of deterministic equations governing the fluid motion.

It is remarkable how the whole complexity of a turbulent flow-field (for instance, fig.2.1) is entirely embedded into the same set of equations that also governs the perfectly ordered motion of a laminar flow.

Statistical approach

As consequence of inevitable small perturbations (in boundary and initial conditions for example), together with an acute sensitivity to these perturbations, different realizations of a same turbulent flow experiment give rise to macroscopically different time histories of any flow variable.

Fig.2.2 shows the record of the streamwise component of velocity in the turbulent wake of a cylinder invested by a uniform flow. The velocity is measured at a fixed location $\mathbf{x}_0$ downstream the cylinder. As it is evidenced in the figure, two different realizations of the same experiment give two different records for the magnitude of the streamwise velocity component. Nonetheless, from the figure it can be envisaged that, even if each realization is different, the mean value of the streamwise velocity component is the same for the two experiments.

More generally, it can be stated that turbulent flow statistics are repeatable (on the contrary, any single actual realization of a turbulent flow-field is not). Consequently, any predictive theory in turbulence shall be statistical in nature. Thus, it is natural to seek for the equations governing the statistics of the flow. Particularly, once that a suitable averaging operator has been defined, the flow-field can be decomposed into its mean and fluctuating

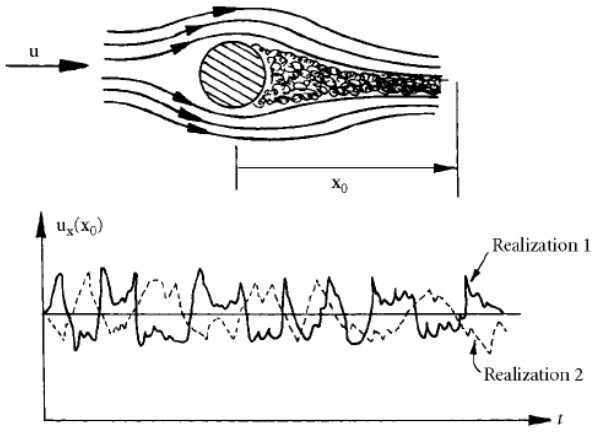

Figure 2.2: *A cylinder is invested by a uniform flow and a turbulent wake forms behind it. The plot represents the records of the streamwise component of velocity at a fixed location downstream the cylinder for two nominally identical realizations. From [5]*

contributions. Namely,

$$\mathbf{u} = \overline{\mathbf{u}} + \mathbf{u}' \tag{2.3}$$

Here the overbar indicates the averaged velocity field and the prime indicates the fluctuation. The application of this decomposition to eq.2.2 and the successive averaging of the result lead to the Reynolds averaged Navier-Stokes equations (RANS) that govern the evolution of the mean flow. In a similar manner, equations are also found for higher order statistics.

Unfortunately, this seemingly hopeful approach has a brief shortcoming: equations for flow statistics are always not closed, meaning that there are more unknowns than equations. As a matter of fact, additional heuristic hypotheses need to be invoked to solve the problem. This is known as the closure problem of turbulence and it implies that any statistical theory, based on this approach, will never be rigorous [5].

Thus, on the one hand, the flow-field $\mathbf{u}$ appears to be random and unpredictable in nature, yet its evolution is always governed by a set of perfectly deterministic equations. On the other hand, statistics of $\mathbf{u}$ are indeed reproducible, but the equations governing their evolution are not known in a closed form.

Numerical simulations

Thanks to the ever growing computational power of modern computers, numerical simulations have become standard practice in engineering applications. In fluid dynamics two different approaches can be distinguished: di-

rect numerical simulations (DNS) and computational fluid dynamics (CFD). The latter is used here to refer to all those numerical methods that aim at finding numerical approximations to the equations governing the statistics of the flow (RANS equations). Due to the closure problem, these methods need to rely heavily on modeling of the unknown terms. Consequently, the accuracy of any result is strongly dependent on the goodness of the closure model. Nonetheless, CFD is still the only available numerical tool when flows of interest for engineering applications come at play. Despite the importance, the present work is not concerned with CFD, but only with DNS.

Conceptually, DNS are easy to understand: starting from a proper initial condition and employing appropriate boundary conditions, Navier-Stokes equations 2.2 are integrated numerically to give a particular realization of the flow-field. However, the computational cost required is extremely high. In fact, accurate and reliable results are obtained only if all the representative scales of motion are resolved appropriately. The flow domain should be large enough to contain eddies of the size comparable to the geometry length-scale and, in the meantime, grid spacing should guarantee that all the dissipative scales of motion are captured. It is well known that separation between these two scales is an increasing function of the Reynolds number. Analogous conclusion applies for time scales: the turn-over time of small dissipative eddies becomes smaller as the Reynolds increases. On the other hand, the flow should be simulated for a sufficiently long time in order to acquire meaningful statistics. As a result, DNS become soon unfeasible for Reynolds number flows of practical interest. However, DNS are a precious tool for turbulent research where they are applied to moderate Reynolds number flows in simple geometries. On this respect, the level of accuracy attained with DNS can hardly be reached by any other experimental technique.

Chapter 3

Flow control

3.1 Movitations

Turbulence has the property of enhancing heat transfer and mixing of mass and momentum. For wall-bounded turbulent flows, increased mixing of momentum in the near-wall region results in a wall shear stress larger than a comparable laminar flow would have.
Turbulence is a highly dissipative phenomenon: at the smallest scales of motion, viscosity performs deformation work that dissipates the kinetic energy of turbulent fluctuations. Thus, if no external energy is supplied, turbulence decays spontaneously. For wall-bounded flows, however, turbulence is not seen to decay, meaning that energy is continuously supplied to turbulence. It turns out that this is done at the expenses of the mean flow. As a consequence, the energy that needs to be spent to drive a fluid through a duct or to push a vehicle through a fluid medium is greater when fluid motion involves turbulence. Enormous savings, in terms of fuel costs and environmental impact, could be achieved if only a proper technology were developed to reduce energy losses due to turbulence. Therefore, research on turbulent drag reduction is a highly active field.

3.2 Coherent structures and wall cycle

Wall-bounded turbulent flows exhibit patterns of coherent motion. An intrinsic difficulty in studying the coherent dynamics of a turbulent flow is that an accepted definition of coherent motion does not exist. According to Robinson [44], it can be defined as a "*three-dimensional region of the flow over which at least one fundamental flow variable exhibits significant correlation with itself or with another variable over a range of space and/or time that is significantly larger than the smallest scale of the flow*". Based on this definition, Robinson provides a useful categorization of coherent structures typically encountered in a turbulent boundary layer in the absence of a mean

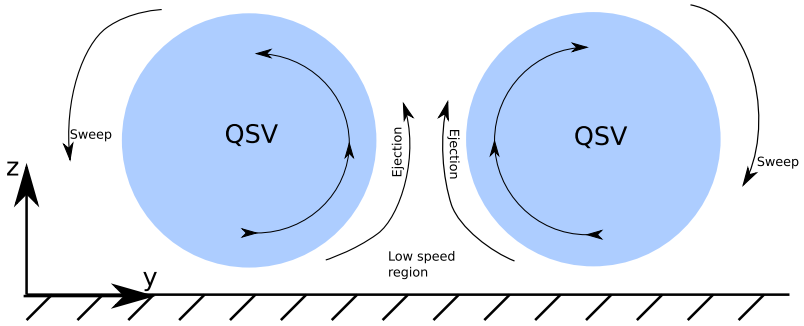

Figure 3.1: *Quasi streamwise vortices, sweeps and ejections*

pressure gradient. Namely, these are:

- Low-speed streaks (LSS) in the viscous sub-layer;
- Low-speed fluid ejections from the wall;
- High-speed fluid sweeps toward the wall;
- Quasi-streamwise vortices (QSV) and other vortical structures of various forms (hairpins, horseshoes).

Experimental and numerical studies of coherent structures have proved the significance of fluid sweeps and ejections in turbulent production (*i.e.* production of turbulent kinetic energy in the near-wall region). Indeed, they are responsible for the high likelihood of negative uw events that contribute positively to the turbulent production $P = -\overline{uw}\frac{\mathrm{d}\overline{U}}{\mathrm{d}z}$ in the buffer region of the turbulent boundary layer.

The dominant vortical structures identified in the near-wall region are the so-called quasi-streamwise vortices (*i.e.* vortical structures whose axis is almost aligned with the mean stream direction). These usually appear as counter-rotating couples and are used to explain both low-speed streaks and fluid sweeps and ejections. As shown in fig.3.1, QSVs are responsible for ejecting low-speed fluid away from the wall and for sweeping high-speed fluid toward the wall. A low-speed region is consequently induced in the space between the two vortices.
LSS which dominate the viscous sub-layer appear as long structures: they are aligned prevalently with the streamwise direction and are spaced constantly with each other. LSS are visualized with help of fig.3.2, where they appear as elongated black areas. In the same figure, grey-colored regions represent vortical structures. Their existence is intuitively explained by the presence of QSV; however, it seems that QSVs do exist because of complex

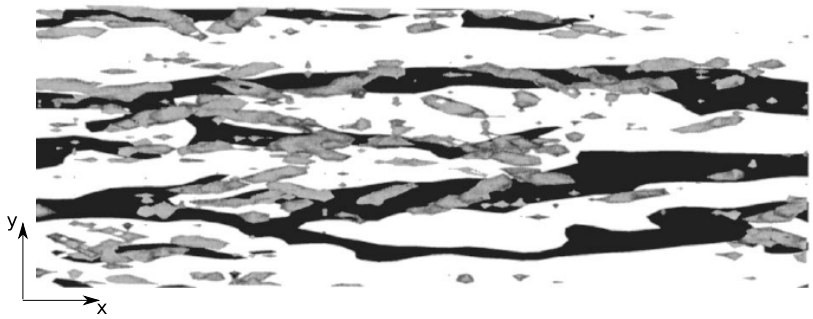

Figure 3.2: *Visualization of low speed streaks (black) and vortical structures (grey). From [45]*

non-linear instabilities that arise during the evolution of LSS. This very complex phenomenon that governs the dynamics of LSS and QSV has been intensively studied and it is called wall cycle. Schoppa and Hussain ([45]) use results of DNS to interpret different mechanisms by which vortical structures (QSV) are generated from LSS. Even though it has not been deeply understood yet, it is accepted that the wall cycle represents the fundamental mechanism by which turbulence can sustain itself at the expenses of the mean flow.

3.3 Flow control strategies

During recent years, significant efforts have been spent on designing efficiently-working flow control strategies for drag reduction. Namely, these can be divided into passive and active strategies. Passive strategies usually employ structured roughness such as riblets to interact with near-wall turbulence and don't require any external energy input. However, maintenance and scalability with Reynolds number pose severe limitations on the applicability of these techniques. Active control strategies, on the other hand, aim at reducing drag by performing some sort of actuation on the fluid flow and consequently need external energy to be supplied. A predetermined control can be implemented, or a more complex feedback control can be used. In the latter case, significant complexity is usually encountered in practical implementations.

The key relation governing the skin-friction drag coefficient for a fully-developed channel/pipe flow can be found by the direct integration of the Navier-Stokes equations [9]. For a plane channel, this results in:

$$C_F = \frac{6}{Re_b} + 6 \int_0^1 (1 - z)(-\overline{u'w'})\, \mathrm{d}z \tag{3.1}$$

This identity indicates that the skin friction coefficient can be divided into two contributions: the first is the well-known laminar contribution, while

the second is a weighted average of the Reynolds shear stress (RSS) $-\overline{uw}$. Being $1 - z$ the weighting (here z is the distance from the wall), the most significant turbulent contribution to the friction drag comes from near-wall RSS. Thus, be the control passive or active, a good strategy should aim at suppressing as much as possible the RSS in the near-wall region. To this end, either passive or active predetermined control using wavy surfaces appear as attractive. A brief review (based on [8]) of flow control strategies with wavy walls is presented in the following sections.

3.4 Passive strategies: compliant surfaces

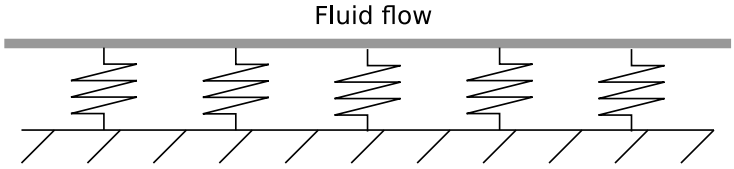

Figure 3.3: *Compliant surface. An isotropic thin plate is suspended by springs attached to a rigid basement*

A compliant surface (or wall) can be defined as a deformable surface whose deformation is passively driven by the adjacent flow. The most straightforward model considers an isotropic compliant surface composed by a thin deformable plate attached to a rigid basement by springs (see fig.3.3). Following [13], the equation governing the vertical displacement η of the plate can be written as:

$$b\rho\frac{\partial^2\eta}{\partial t^2} + d\frac{\partial\eta}{\partial t} + B\frac{\partial^4\eta}{\partial x^4} - T\frac{\partial^2\eta}{\partial x^2} + K\,\eta = f \tag{3.2}$$

Where b is the plate thickness, ρ is the plate density, d represents the damping, B is the flexural rigidity of the plate, T is the pre-stress longitudinal tension, K represents the stiffness of the springs and f is the wall-normal stress induced by the adjacent fluid-flow. Namely, f is a forcing produced by the pressure and normal stresses fluctuations. More cumbersome models exist, involving anisotropic plates and non-orthogonal oriented springs [3]. A compliant surface, coupled with turbulent flow, usually undergoes deformation in the form of streamwise traveling waves [27]. In [11], this wall deformation is seen to be effective in producing near-wall regions with negative distributions of Reynolds shear stress. However, in that study, only small drag reduction rates were achieved (8%).

In general, designing a compliant surface, capable of interacting favorably with the near-wall turbulence, requires the determination of all parameters in eq.3.2 so that the characteristic frequency of the plate matches that of turbulence [8].

Despite the evident advantages (*i.e.* no external power required), intensive DNS studies ([7], [11]) have been performed and proved that drag reduction effect by passive compliant surfaces is marginal, non-universal and still questionable.

3.5 Active strategies: streamwise traveling waves of blowing and suction

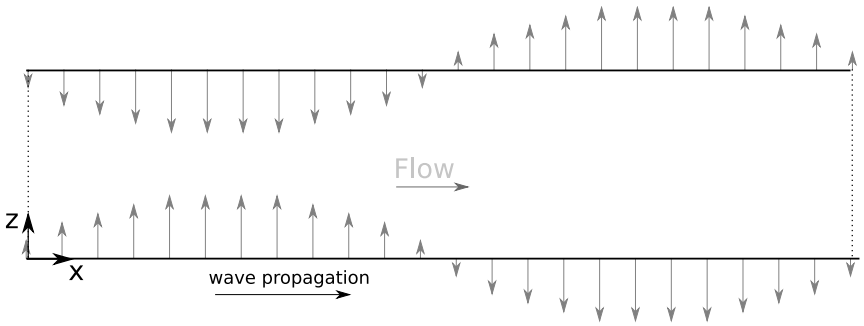

Figure 3.4: *Blowing and suction streamwise traveling wave*

The control strategy of traveling waves of blowing and suction was first proposed by Min *et al.* in [31] based on the implication of the identity 3.1.

Actuation at the wall consists in prescribing a wall-normal velocity in the form:

$$w = a\,cos[k(x - c\,t)] \tag{3.3}$$

Where a represents the wall-velocity amplitude, k the wave number and c is the phase speed. Both the upper and lower walls of the channel are fixed and rigid; a sketch of the geometry is presented in fig.3.4.

A linear analysis, equivalent to that in [31], is reported by Mamori *et al.* in [29]. They consider a base laminar flow subject to small perturbations. A drag increment is predicted by inserting first-order solutions inside the eq.3.1. Namely, drag reduction is found for all upstream traveling waves. Since the reference condition is a laminar flow, it is asserted that sub-laminar drag can be achieved for a flow at a fixed bulk Reynolds number. However, it is recalled that the net power required for pumping and controlling the flow always exceeds that of the base flow (as proved in [12] and [1]).

In the absence of a base flow, traveling waves of blowing and suction always determine a net pumping from the wall in the direction opposed to the wave propagation ([16]). Pumping is generated by the combined action of wall actuation and a viscous effect. The former entrains fluid particles into a circular motion, while the latter is responsible for an asymmetry in the forward and back motions of the fluid particle. This asymmetry has

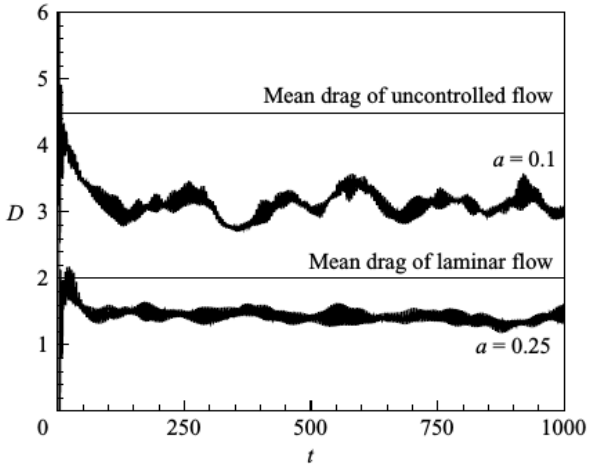

Figure 3.5: *Friction drag reduction by upstream traveling waves. From [31]*

the overall effect of producing a net pumping in the direction opposed to the wave propagation. Hoepffner and Fukagata also provide a temptative mechanism for relating drag reduction with this pumping effect. Namely, for an upstream traveling wave, a net flux in the downstream direction is produced by the pumping. As a consequence, the mean pressure gradient required to drive the flow at a constant rate is reduced. Further, the spatial average of the RSS, weighted by the distance from the wall, is proportional to the mean pressure gradient ([10]). Hence, the pumping-induced reduction in the mean pressure gradient reflects as a weakening in the RSS distribution in the near-wall region and, ultimately, in a weakening of turbulent production.

The efficacy of traveling waves of blowing and suction is also confirmed for fully turbulent flows in [31]. In fig.3.5 it is shown the effect of two different upstream traveling waves on the friction drag D. However, the stability analysis of Lee *et al.* [23] shows that upstream traveling waves (*i.e.* those determining also sustained sub-laminar drag) do not promote the stability of the flow. On the contrary, downstream traveling waves with a phase speed exceeding the centerline velocity are found to have a stabilizing effect. Further investigations by Moarref and Jovanovic [33] and by Lieu *et al.* [25] reveal that the stabilizing effect of downstream traveling waves can be exploited to relaminarize a turbulent channel flow.

The parametric study of Mamori *et al.* [30] explores the range of parameters of the traveling waves of blowing and suction. Maps of the drag reduction rate relative to Re_τ = 110 and Re_τ = 300 is shown in fig.3.6. For downstream waves ($c > 0$) large drag reduction rates can be attained for proper ranges of wavelengths. Further, Mamori *et al.* point out that, for certain sets of parameters, downstream traveling waves lead to a stable relaminarization of the flow.

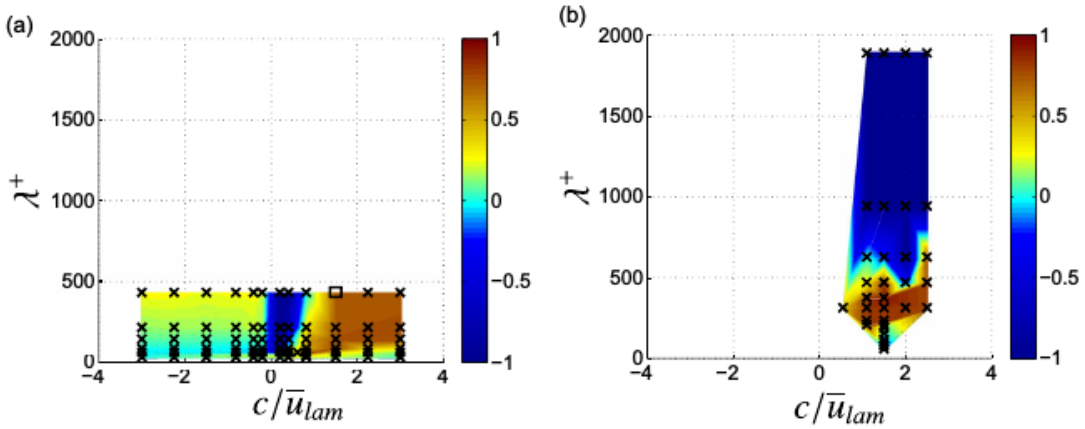

Figure 3.6: *Drag reduction rate as function of wave parameters. λ is the wave-length and $\overline{u}_{lam}$ is the bulk velocity of the laminar flow. (a) $Re_\tau = 110$; (b) $Re_\tau = 300$. From [30]*

3.6 Active strategies: streamwise traveling waves of wall deformation

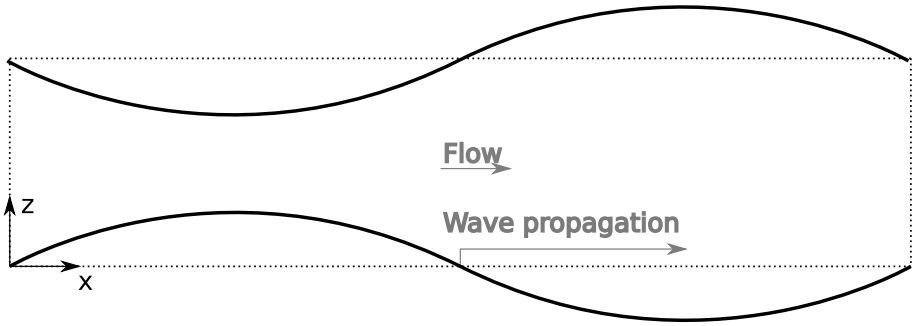

Figure 3.7: *Streamwise traveling wave of wall deformation*

Results obtained with traveling waves of blowing and suction are attractive. Nonetheless, the implementation of actual devices is still complicated with the available technology. A seemingly hopeful alternative could be that of replacing waves of blowing and suction with traveling waves of actual wall deformation (fig.3.7). In the latter case, walls could be driven by a smaller number of actuators.

In the analysis of Hoeppfner and Fukagata [16] a pumping effect, induced by wall actuation, is observed for streamwise traveling waves of wall deformation. The pumping acts in the same direction as the wave propagates: a downstream traveling wave produces pumping in the downstream direction.

Recalling the effect of the pumping phenomenon (suggested in [16] and explained in the previous section), it is natural to expect drag reduction for downstream traveling waves. Further, stability analyses [23], [33] and [25] suggest that downstream traveling waves should promote the stability of the flow.

First observations of the beneficial effects on friction drag of traveling waves of wall deformation are found in the experimental work of Taneda and Tomonari [48]. They study the turbulent boundary layer that develops over a moving wavy surface in connection with the swimming motion of fishes. Mainly, they found that for phase speeds exceeding the external uniform stream velocity, the flow tends to laminarize (locally).

Also related to the swimming motion of fishes is the work of Shen *et al.* [47]. They study the turbulent boundary layer over a traveling wavy wall for different phase speeds. Namely, they confirm the positive effect on turbulence suppression promoted by waves whose speed exceeds the mean velocity of the external flow. However, they emphasize that this is a local

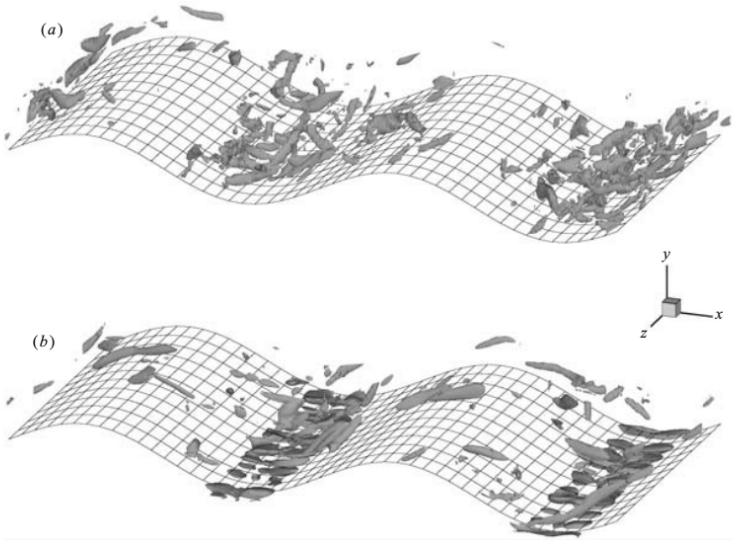

Figure 3.8: *Vortex structure.* $\frac{c}{U} = 0$, *(a);* $\frac{c}{U} = 1.2$, *(b). From [47]*

effect, as can be observed in fig.3.8. The figure shows vortex structures for a stationary (fig.3.8(a)) and a moving wave (fig.3.8(b)).

A recent parametric study of traveling waves of wall deformation is reported by Nakanishi *et al.* in [35]. They consider a reference plane channel flow at $Re_\tau = 180$ driven at a constant flow rate. The control is enforced through:

$$w = a\,cos[k(x - ct)] \quad at \quad z = -\frac{a}{kc} sin[k(x - ct)] \tag{3.4}$$

Here a is the wall velocity amplitude, k is the wave number and c is the

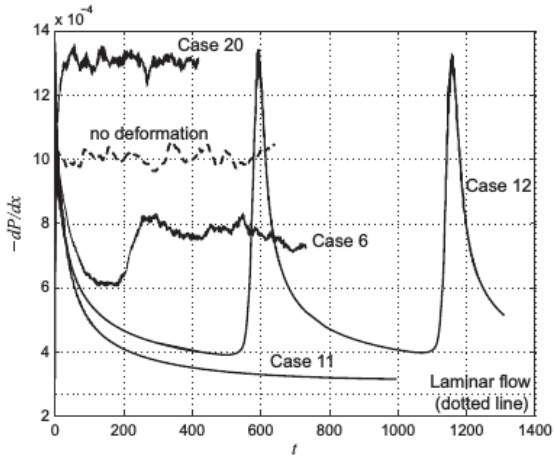

Figure 3.9: *Time traces of the mean pressure gradient found in [35]*

phase speed. Only in-phase motion is considered for the lower and upper walls of the channel (peristalsis). The deformation amplitude $\frac{a}{kc}$ is always comparable to the thickness of the viscous sub-layer of the uncontrolled flow. As stressed out in [16], this is a necessary condition for attaining the pumping effect induced by wall actuation. As expected, drag reduction is achieved for all the downstream traveling waves ($c > 0$) while a drag increase is attained for upstream traveling waves ($c < 0$). The parameter used to ascertain drag reduction is the mean pressure gradient used to force the flow through the channel at a constant rate. Fig.3.9 depicts the time traces of the mean pressure gradient of some specific cases reported in [35]. In the figure four different behaviors are evidenced. Starting from above, it can be stated that (curves in the figure should be compared to the *no deformation* case):

- *case* 20 (upstream wave, $c < 0$) determines a drag increase;
- *case* 6 (downstream wave, $c > 0$) determines a drag reduction;
- *case* 11 (downstream wave, $c > 0$) determines a significant drag reduction (close to the laminar value);
- *case* 12 (downstream wave, $c > 0$) is unstable.

Of particular interest is *case* 11: in this case, not only drag reduction is achieved, but the flow is seen to relaminarize during the simulation. This can also be noticed by the close value of the mean pressure gradient to the laminar limit (depicted in the figure by a dotted line).

Chapter 4

Numerical method

The numerical method, as well as the programming language used for its implementation, was first conceived and developed by Paolo Luchini. This numerical strategy offers a new way of dealing with immersed boundaries on a non-body-conforming cartesian grid, retaining great simplicity of implementation and good parallel scaling features. The same code has already been validated with existing data in the literature and proven to be reliable when dealing with immersed non-moving boundaries. The extension to the more general case of moving boundaries is the primary concern of the present work and will be explained in what follows. More precisely, this section focuses on the description of the numerical technique with particular attention to the general moving boundaries case and the issues that naturally arise with it.

4.1 Governing equations

The reference geometry considered is that of a plane channel flow, i.e., a flow confined between two flat walls of infinite extension separated by a distance of $2\delta^*$ (fig.4.1). Here and in what follows, an asterisk is used to denote physical quantities expressed in dimensional form. The flow is assumed to be unsteady, viscous and incompressible, thus, Navier-Stokes equations, in non-dimensional form, read:

$$\frac{\partial u_j}{\partial t} + \frac{\partial u_i u_j}{\partial x_i} + \frac{\partial p}{\partial x_j} - \frac{1}{Re}\frac{\partial^2 u_j}{\partial x_i x_i} = F_j \quad j = 1,2,3 \tag{4.1a}$$

$$\frac{\partial u_i}{\partial x_i} = 0 \tag{4.1b}$$

where x_i are the Cartesian coordinates, u_i are the corresponding velocity components, p is the pressure, F_j is a forcing term and Re is the Reynolds number defined as $Re = \frac{U^* h^*}{\nu^*}$. Note that summation is implied over all repeated indices. Here, $x_1 = x$, $x_2 = y$ and $x_3 = z$ coordinates are aligned,

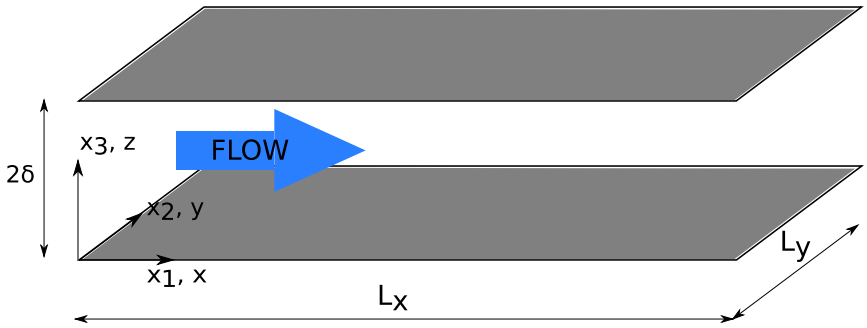

Figure 4.1: *Reference channel flow geometry*

respectively, with the streamwise, spanwise and wall-normal directions. All physical variables are non-dimensionalized using an appropriate velocity U^* and a length reference scale h^*. Particularly, lengths in eq.4.1 are made dimensionless using the half channel height so that the reference length scale h^* appearing in the Reynolds number definition corresponds to δ^*. The forcing term F_i appearing in eq.4.1 is needed to drive the flow through the channel and, hence, it is assumed that only F_1 is different from zero since the mean flow is aligned with the streamwise coordinate. According to [41], three different approaches can be employed for the simulation of turbulent flows through channels; namely these are constant flow-rate (CFR), constant pressure gradient (CPG) and constant power input (CPI) strategies. The first two are, by far, the most popular, while the latter represents quite a novelty introduced in [15]. In a CFR simulation, the forcing F_1 is found from the uniform (in space) mean pressure gradient that needs to be adjusted, at each time instant, to keep the flow-rate at a prescribed value. On the other hand, with the CPG approach, the flow is driven by a constant (in time) mean pressure gradient, while the flow-rate is left free to change. Finally, in the CPI strategy, what is kept constant is the product of flow-rate and mean pressure gradient. In the present study, the CFR approach is adopted; as explained in [41], a natural choice when dealing with constant flow-rate simulations is to choose, as reference velocity U^*, the mean bulk velocity U_b^*. The same choice is made here, so that all the velocities components in eq.4.1 are made dimensionless using U_b^* and the Reynolds number corresponds to $Re_b = \frac{U_b^* \delta^*}{\nu^*}$.
The reference geometry in fig.4.1 depicts a channel confined by two flat walls; however, in general, solid boundaries of the channel will be represented by arbitrary non-planar and, possibly, time-dependent surfaces on which no-slip boundary conditions must be enforced. Moreover, the computational domain measures L_x and L_y in the streamwise and spanwise directions respectively, where periodic boundary conditions are also applied to simulate the infinite extension of the channel.

Finally, eq.4.1 must be coupled with a proper initial condition which, in the present code, may be given either as an external input flow field or directly initialized at the beginning of the simulation by the code itself. In the latter case, the initial velocity profile is laminar.

4.2 Discretization

Spatial discretization

One of the main advantages given by the immersed boundary technique is the fact that, for such methods, solid boundaries are fully immersed within the computational grid that, therefore, is not body fitted (*i.e.* grid nodes don't lie on the surface of the boundaries). As a consequence, grid generation is made trivial, and it is performed once and for all at the beginning of a simulation. The code presented here takes advantage of this feature and performs the spatial discretization of eq.4.1 on a fixed Cartesian grid using standard second order-accurate centered finite differences. Furthermore, the code collocates fluid-dynamic variables in a staggered fashion within the computational domain. This approach is the same as considering two distinct non-overlapping grids shifted of half grid-spacing from each other. An example is shown in fig.4.2 for a bidimensional case. Staggered grids are standard practice when dealing with the numerical approximation of Navier-Stokes equations using finite differences schemes on Cartesian grids ([36]).

Uniform spacing is adopted for streamwise and spanwise directions, while clustering is possible for the wall-normal direction. Such characteristic is exploited to save memory during execution: only wall-normal coordinates are stored, while streamwise and spanwise locations are easily computed whenever needed.

Time advancement

Numerical integration of governing equations is performed using a fractional step approach. More precisely, within a given time-step, the momentum equation (eq.4.1a) is first advanced in time without taking care of the incompressibility constraint (eq.4.1b). The latter is enforced during the so-called projection step: the velocity field gets projected onto the solenoidal vector-field, and, in the meantime, the pressure is updated accordingly.

The time-scheme chosen for time advancement is a fully explicit third-order Runge Kutta method; the time-step is divided into three sub-steps, during which the fractional step technique is applied independently. Hence, the procedure can be summarized as follows:

given the velocity $\mathbf{u}^k_{ix,iy,iz}$ at the sub-step k, at a grid location (ix, iy, iz),

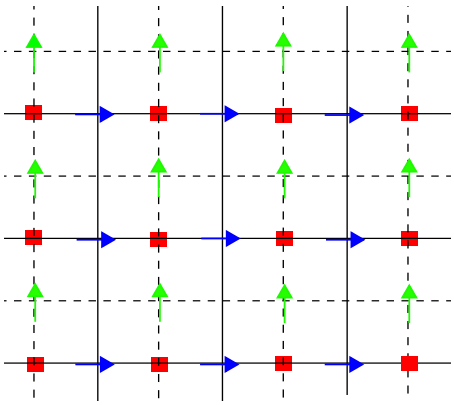

Figure 4.2: *Example of 2D staggered grid. Red squares pressure, blue and green arrows velocity components*

the intermediate velocity $\hat{\mathbf{u}}^{k+1}_{ix,iy,iz}$, at the next sub-step $(k+1)$, is found:

$$\begin{aligned}\hat{\mathbf{u}}^{k+1}_{ix,iy,iz} =& \mathbf{u}^{k}_{ix,iy,iz} + \alpha_k \Delta t\, LNL(\mathbf{u}^{k}_{ix,iy,iz}) + \beta_k \Delta t\, LNL(\mathbf{u}^{k-1}_{ix,iy,iz}) + \\ & (\alpha_k + \beta_k)\Delta t \left[\mathbf{F}^k - \mathbf{G}(p^k)\right]\end{aligned} \tag{4.2}$$

where α_k and β_k are the coefficients of the Runge Kutta method and $LNL(\cdot)$ is the operator containing the linear $L(\cdot)$ and non linear $NL(\cdot)$ disctretized operators of eq.4.1a (namely, $LNL(\cdot) = L(\cdot) + NL(\cdot)$). Linkewise, $\mathbf{G}(\cdot)$ is the discretized gradient operator. The intermediate velocity, computed using eq.4.2, is then projected onto the field of divergence-free vectors using:

$$\mathbf{u}^{k+1}_{ix,iy,iz} = \hat{\mathbf{u}}^{k+1}_{ix,iy,iz} - \mathbf{G}(\phi^{k+1}_{ix,iy,iz}) \tag{4.3}$$

where the pseudo-pressure ϕ is found from the numerical solution of the following Poisson equation:

$$\nabla^2 \phi^{k+1} = \nabla \cdot \hat{\mathbf{u}}^{k+1} \tag{4.4}$$

The linear system that arises from the discretization of eq.4.4 is solved employing a fast iterative in-line SOR technique. Finally, the pressure field is updated using:

$$p^{k+1}_{ix,iy,iz} = p^k + \frac{\phi^{k+1}_{ix,iy,iz}}{(\alpha_k + \beta_k)\Delta t} \tag{4.5}$$

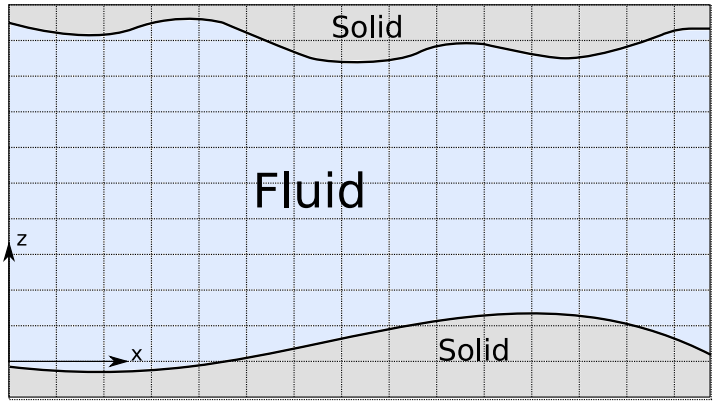

Figure 4.3: *Example of solid boundaries immersed within a fixed Cartesian grid*

4.3 Immersed solid boundaries

IB techniques

Immersed boundary (IB) methods refer to a broad family of numerical strategies conceived for simulating the presence of boundaries inside a fluid domain. One of the first appearances of these techniques is due to C. Peskin who, in [37], introduces an IB procedure for the 2-dimensional calculation of blood flow inside mitral valves. Since then, a large variety of methods have been proposed for studying fluid-flow phenomena of different nature; typical applications are simulations of the interaction of fluids with solid rigid bodies (for instance [52], [50], [49]) or elastic bodies ([37], [38]) and multi-phase flows ([40]).
The basis on which these methods stand is that physical boundaries are immersed within a fixed Cartesian, non-body-conformal, grid. An example can be visualized in fig.4.3. A particular procedure is then employed to enforce boundary conditions, and this usually requires a modification of the governing equations in the close vicinity of an interface. An apparent advantage is that mesh generation becomes an easy task, as it can be performed once and for all at the beginning of a calculation, without caring about neither the location nor the complexity of the boundary.

On the other hand, for numerical methods that rely on standard body-conformal grids, mesh generation requires, usually, a significant computational effort and involves either complex coordinates transformation or cumbersome discretization operators. On this respect, the advantage brought about by IB strategies is even more evident when dealing with non-stationary boundaries as, for standard body-fitted methods, grid generation must be performed at each time-step. Conversely, grid resolution may have a better behavior for body-conformal meshes rather than Cartesian grids. As stated

in [18], when geometries with steep gradients and high curvatures are involved local grid refinement cannot be performed with Cartesian methods. This has severe consequences on how grid size scales with Re number. As explained in [32], it can be shown that the ratio of Cartesian to body-fitted grid sizes is of the order $O(\frac{L}{\delta})^2$, where L is a representative length-scale of a solid body, and δ is the boundary layer thickness. Since δ increases with increasing Re, the ratio becomes very large for high Re number flows and, consequently, a given resolution would require an exceedingly large Cartesian grid. It is also stressed out that this fact does not directly imply a higher computational cost because, as the size of the grid increases, a more significant number of mesh nodes lies inside the body and, therefore, the calculation is not needed for an increasingly larger number of points. Of course, this depends on the considered geometry and nothing general can be stated.
Even though significant differences exist among all the available IB methods, a common feature is that interfaces between fluids and solids (or between different fluids) are mimicked by introducing a forcing term inside the governing equations. More specifically, following [32], IB techniques can be broadly divided into two categories based on the forcing being applied either to the continuous or discrete form of the governing equations. Methods falling in the first group are well suited for simulating fluid flows interactions with elastic bodies while they usually give rise to stiff problems when applied to flows around rigid moving boundaries.

Boundary conditions on solid moving walls

The numerical code, used in this study, implements a fairly innovative IB strategy that applies no-slip boundary conditions on solid walls through a correction of the governing equations in their discrete form. The same technique was proven to be successful for the simulation of flows over stationary wavy walls [26]. The present work aimed to extend this IB methodology to the case of moving walls; an explanation of the general boundary treatment is reported in the following.

In the current implementation, solid boundaries are represented by the upper and lower walls of the channel, as in fig.4.3. It is assumed that the shape of the two walls is known in analytical form. Hence, at any time instant, the solid boundary of the channel is defined by:

$$\begin{cases} z = \eta_l(x, y, t) & lower\,wall \\ z = \eta_u(x, y, t) & upper\,wall \end{cases} \tag{4.6}$$

In the present study, the walls of the channel are free to move only in the z direction (*i.e.* in the wall-normal direction of the reference channel in

fig.4.1). The velocity of a point lying on the surface of the boundary is given by:

$$\begin{cases} \boldsymbol{U}_l = w_l(x,y,t)\,\hat{\boldsymbol{z}} & lower\,wall \\ \boldsymbol{U}_u = w_u(x,y,t)\,\hat{\boldsymbol{z}} & upper\,wall \end{cases} \tag{4.7}$$

Where w_l and w_u are the time-derivatives of η_l and η_u, respectively, and $\hat{\boldsymbol{z}}$ is the unit wall-normal vector.

No-slip boundary conditions are applied at the solid boundary of the channel; with respect to a fixed frame of reference, the velocity of the fluid at a given point on the solid boundary must equal the velocity of the boundary at the same point. More precisely:

$$\begin{cases} u(x,y,z,t) = v(x,y,z,t) = 0\,;\, w(x,y,z,t) = w_l(x,y,t) \quad at \quad z = \eta_l(x,y,t) \\ u(x,y,z,t) = v(x,y,z,t) = 0\,;\, w(x,y,z,t) = w_u(x,y,t) \quad at \quad z = \eta_u(x,y,t) \end{cases} \tag{4.8}$$

In the present numerical method, boundary conditions 4.8 are enforced on the intermediate velocity $\hat{\mathbf{u}}$ during time advancement of the momentum equation 4.2. This imposition is straightforward for all grid points lying precisely on the immersed boundary. However, the grid is Cartesian and non-body-conformal, thus grid nodes rarely lie on the boundary surface. The procedure applied for the fulfillment of condition 4.8 is presented in the following.

IB procedure: a two-dimensional example

It is helpful to consider a two-dimensional example of a channel where a non-null vertical velocity is prescribed at the solid boundary. At first momentum equation is advanced in time, using eq.4.2, for all grid nodes inside the fluid domain, without taking into account no-slip boundary conditions. For the sake of simplicity, the explicit Euler method will be used in place of the Runge-Kutta method. Consider the grid node (ix, iz) in fig.4.4. The vertical velocity w at time-step $n+1$ is computed as:

$$\tilde{w}^{n+1}_{ix,iz} = w^n_{ix,iz} + \Delta t \left[L(w^n_{ix,iz}) + NL(w^n_{ix,iz}, w^n_{ix,iz}) - G_z(p^n_{ix,iz}) \right] \tag{4.9}$$

Here, a $\sim$ indicates that the velocity in eq.4.9 is advanced without enforcing the boundary condition $w = W_{IB}$ on the boundary. In fact, all terms inside the square brackets are computed without accounting for the exact location of the boundary interface. To overcome this inconsistency, a corrective term is applied to eq.4.9; further, based on the fact that very close to a solid wall the leading contribution to momentum balance is due to the viscous term, a correction is applied only to the linear term $L(\cdot)$. If the grid-node of $w_{ix,iz}$ lied precisely on the boundary surface, discretization of the viscous term of

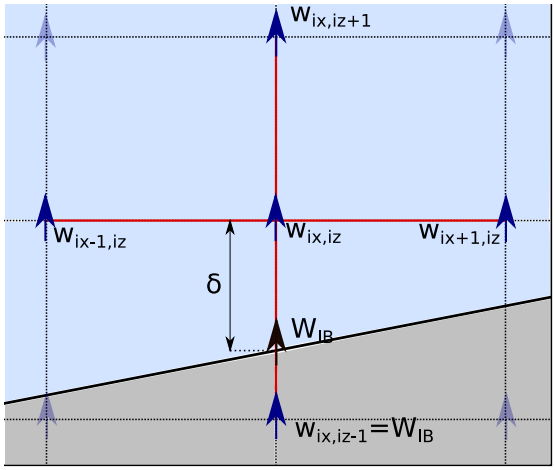

Figure 4.4: *Numerical stencil intersecting the solid boundary*

eq.4.1 would read:

$$L(w_{ix,iz}) = \frac{1}{Reb}\left[\frac{w_{ix-1,iz} + w_{ix+1,iz}}{\Delta x^2} + \frac{W_{IB} + w_{ix,iz+1}}{\Delta z^2} - \left(\frac{2}{\Delta x^2} + \frac{2}{\Delta z^2}\right) w_{ix,iz}\right] \tag{4.10}$$

However, this is incorrect because eq.4.10 does not account for the actual location of the boundary. Conversely, a more appropriate way of computing $L(w_{ix,iz})$ is:

$$L(w_{ix,iz}) = \frac{1}{Reb}\left[\frac{w_{ix-1,iz} + w_{ix+1,iz}}{\Delta x^2} + \frac{W_{IB}}{\delta \Delta z} + \frac{w_{ix,iz+1}}{\Delta z^2} - \left(\frac{2}{\Delta x^2} + \frac{1}{\Delta z^2} + \frac{1}{\delta \Delta z}\right) w_{ix,iz}\right] \tag{4.11}$$

The correction C is added to eq.4.9 in the form:

$$w_{ix,iz}^{n+1} = \tilde{w}_{ix,iz}^{n+1} - \Delta t C \tag{4.12}$$

where C is deduced by comparing eq.4.10 with eq.4.11. The correction can be written in the form:

$$C = c_1\, w_{ix,iz} - c_2\, W_{IB} \tag{4.13}$$

Where, in this particular example:

$$c_1 = c_2 = \frac{1}{Reb}\left(\frac{1}{\delta \Delta z} - \frac{1}{\Delta z^2}\right) \tag{4.14}$$

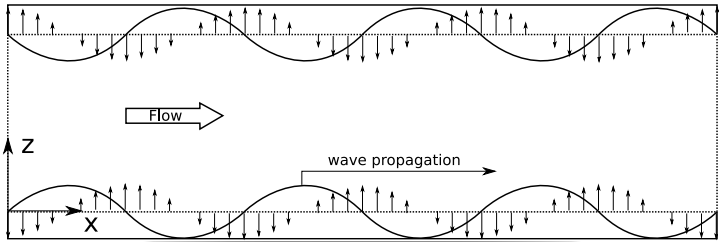

Figure 4.5: *Channel flow confined between two streamwise-traveling waves of wall deformation. Arrows represent wall velocity*

Furthermore, the correction 4.13 is conveniently computed using the velocity field already updated at time-step $n+1$, so that eq.4.12 can be solved directly for $w_{ix,iz}^{n+1}$:

$$w_{ix,iz}^{n+1} = \frac{\tilde{w}_{ix,iz}^{n+1}}{1 + c_1 \Delta t} + \frac{c_2 \Delta t}{1 + c_1 \Delta t} W_{IB} \tag{4.15}$$

It should be noticed that, as $\delta \to 0$ (*i.e.* as the point (ix, iz) lies closer and closer to the boundary), the term $c_1 = c_2 \to \infty$ and, therefore, the first term on the right hand side of eq.4.15 tends to vanish while the second one approaches the boundary velocity W_{IB}. On the other hand, if $\delta = \Delta z$, then the point $(ix, iz-1)$ lies exactly on the boundary and no correction is applied (as $c_1 = c_2 = 0$).

The extension to the three-dimensional case is quite straightforward. It should be stressed out that the IB treatment just explained requires only the knowledge of the relative distance grid-node - boundary for all the nodes whose numerical stencil intersects the boundary. Naturally, this information must be updated at each time-step in the case of non-stationary walls.
Another remark is that corrective coefficients differ for each component of the velocity if discretization is performed on a staggered grid. In fact, in that case, the numerical stencil is distinct for each velocity component.
As previously explained, the original numerical code was conceived for the simulation of flows over stationary walls; this situation is readily recovered in eq.4.15 by simply setting $W_{IB} = 0$.

4.4 Issues with moving boundaries

In the view depicted so far, a solid rigid boundary is immersed within the frame of a fixed staggered Cartesian grid and, if a motion is prescribed, it moves changing its position relative to grid nodes. An issue that usually appears with IB methods for simulating fluid-flows interactions with non-stationary rigid solid bodies is the birth of spurious force oscillations [28], [46] and [24].

This problem was also experienced with the numerical procedure used

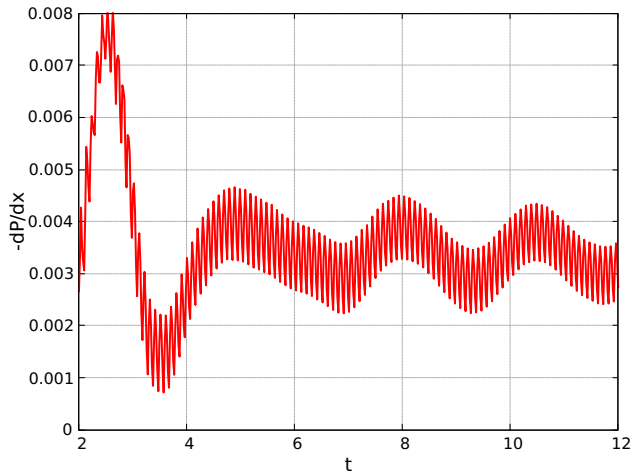

Figure 4.6: *Observed oscillations in the mean pressure gradient*

in the present work. Mainly, temporal fluctuations in the mean pressure gradient were observed. For instance, consider the channel configuration reported in fig.4.5 where the flow is confined by two streamwise-traveling waves of wall deformation. This is a particular example of the flow-control strategy presented in the next chapter. The time trace of the mean pressure gradient that drives the flow is represented in fig.4.6 for wall-actuation parameters: deformation amplitude $h = 0.1$, wall-velocity amplitude $a = 0.4$, wave-number $k = 2$ and phase-speed $c = 2$. Grid employed in the example is $nx = 256$ (streamwise), $ny = 128$ (spanwise) and $nz = 96$ (wall-normal); time-step size $\Delta t = 0.0196$. Large amplitude oscillations are clearly visible in the figure.
Following [24], oscillations in computed flow variables should be attributable to the fact that, during the motion of the immersed-boundary, grid nodes get continuously either covered or cleared by the solid boundary. In return, this is likely to cause:

- a temporal discontinuity of velocity for grid nodes that get covered by wall motion;
- a spatial discontinuity of pressure for nodes that get freed by wall motion

However, both these possibilities have been checked with the present numerical technique and no effect was observed on oscillations. As a matter of fact, the method allows for a smooth transition velocity nodes that get covered by the wall; on the other hand, pressure nodes were also found to have no influence on observed fluctuations.
Another possible source of oscillations is reported in [46], where it is pointed out that fluid-volume conservation is the primary cause of spurious temporal

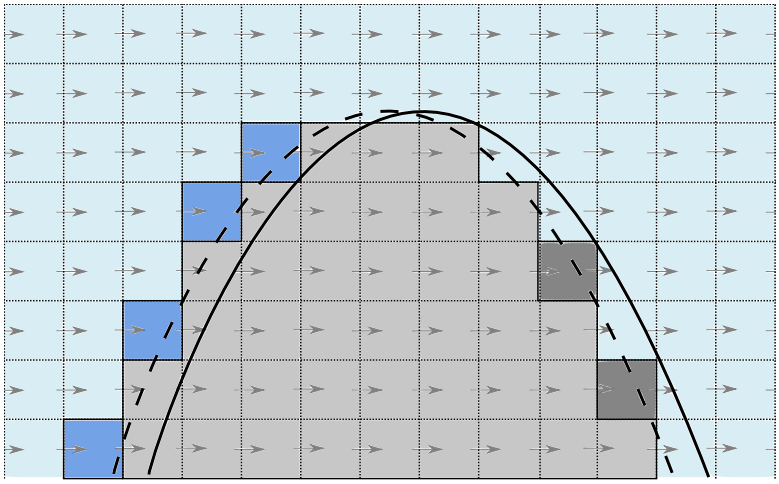

Figure 4.7: *Fluid volume variation due to boundary motion. Boundary at:* - - - - -*, t;* ———*, $t + \Delta t$. Light blue, fluid; blue, freshly cleared cells; grey, solid boundary; dark-grey, freshly covered cells*

oscillations in fluid-dynamic variables. Indeed, as the solid boundary moves, a variable number of grid cells gets either cleared or covered by it, giving rise to instantaneous variations of the total fluid volume. This inconvenience has a straightforward solution for finite volume methods, as it is easier to enforce volume conservation for each numerical cell cut by the boundary [21]. On the other hand, for finite differences schemes, it is less clear how to assure the enforcement of this constraint. Nonetheless, an ad-hoc solution for the cases studied in this work has been found by merely setting a restriction on the time-step size. Consider the situation represented in fig.4.7; it is assumed that a numerical cell belongs to the fluid-phase if its u-velocity node lies outside the solid wall. Thus, cells in the figure are colored according to this definition. Now, during a time-step of arbitrary size, wall motion clears and covers a different number of velocity nodes, hence varying the total of cells considered in the fluid region. Fig.4.7 should clarify this situation. Since wall motion is known a priori, the time-step size can be chosen so that, for a given grid-spacing, wall movement clears and covers the same number of velocity nodes during each temporal iteration. More precisely, for a sinusoidal wave of wall deformation, traveling at a phase speed c, the following condition must be satisfied:

$$\frac{c\Delta t}{\Delta x} = n \tag{4.16}$$

where n is an integer greater than one and Δx is the streamwise grid-spacing. The effect of this choice on the time trace of the mean pressure gradient of the previous example is shown in fig.4.8.

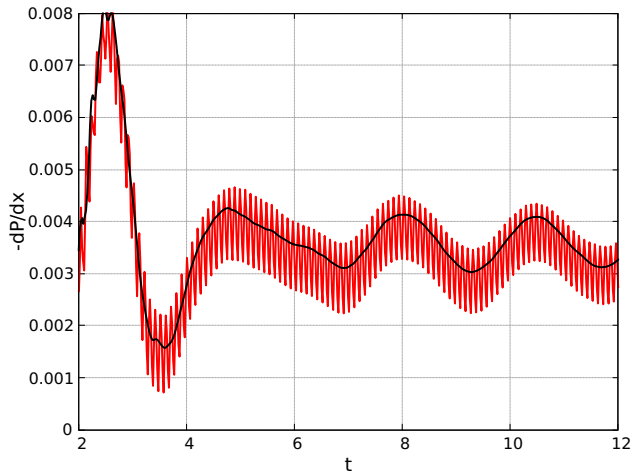

Figure 4.8: *Effect of the choice of the condition 4.16 on spurious oscillations.* ——, *arbitrary* Δt; ——, $\Delta t = \frac{\Delta x}{c}$

Even though condition 4.16 sets a strict limitation, space is left for tuning of grid resolution and temporal accuracy. Nonetheless, this artifice cannot be considered a general solution to the problem, as a condition in the form of 4.16 can't be found for a more complex wall motion. Thus, an essential task for future development is that of finding a new way to overcome the issue.

4.5 Code structure

The numerical method reviewed in the previous sections is implemented in the CPL programming language (a high-level language conceived and developed by Paolo Luchini for his own research). The code is very concise and consists of four different files, namely:

- `undwall.cpl`
- `timestep.cpl`
- `iofiles.cpl`
- `parallelbcs.cpl`
- `parallelbcs.h`

The main script is `undwall.cpl`; it contains the time-loop through which temporal iteration is performed. At each cycle the following tasks are successively executed:

- coefficients for the IB method are computed, using the subroutine `calcimbc`, based on the position of the walls at the current time-step;
- the sub-steps of the Runge-Kutta method are performed through three consecutive calls at the subroutine `timestep`;
- output is printed out; this consists of current iteration, external time, mean pressure gradient in the streamwise and spanwise directions and the current Courant number;
- finally, the current flow-field is (possibly) saved.

The subroutine `calcimbc`, used for the computation of the IB coefficients, is defined inside the file `undwall.cpl`. Its original version allowed only the treatment of the lower wall of the channel, and thus, an extension was developed for this study to allow arbitrary shapes for both the top and lower walls. In practice, the subroutine uses two separate boolean functions (one for each wall) that return a true value if a given grid-point lies inside the boundary. This requires the shape of both walls to be known in analytical form. At each call to `calcimbc`, IB coefficients are computed for all the solid boundaries and are stored in 2-dimensional arrays whose elements are pointers to 1-dimensional arrays and whose size corresponds to the extension of the grid in the $x-y$ plane. Therefore, at each (ix, iy) location, a 1-dimensional array stores the coefficients for all those grid-nodes (in the undeformed-wall normal direction) in the fluid-phase whose numerical stencil intersects the boundary. Three separate arrays are needed for each wall: one per velocity component. It must be stressed-out that IB coefficients must be updated at each time-step when non-stationary boundaries are considered, while the case of fix walls requires this computation only at the beginning of the simulation.

The file `timestep.cpl` contains the subroutine responsible for time marching named, as a matter of fact, `timestep`. The latter has a quite general form, in the sense that it requires as input only another subroutine which specifies the numerical scheme used for time advancement. Tasks performed by `timestep` are as follows:

- time advancement of the momentum equation through the subroutine `linestep`;
- projection of the intermediate velocity field onto the space of solenoidal vectors and pressure update through the `pressurelinestep` subroutine;
- correction of the velocity field in order to guarantee a constant flowrate and corresponding update of the mean pressure gradient needed to drive the flow.

More precisely, `linestep` advances momentum equation for all the velocity components and all grid nodes (in the fluid-phase) at a fixed location in the $x-y$ plane. An external loop, defined in the core of the subroutine `timestep`, calls `linestep` for all grid-locations in the horizontal plane and, hence, velocity update is achieved for all points.
On the other hand, `pressurelinestep` implements an efficient in-line SOR algorithm for the iterative solution of the linear system arising from the discretization of eq.4.4. The unknown scalar field ϕ is arranged following a red-black ordering in the $x-y$ plane; an external loop, defined in the `timestep` subroutine, cycles successively on all black and red locations for a user-defined number of times. Thanks to this sorting (as a matter of fact, red-black columns in the horizontal plane), updating the column of unknowns at a location (ix, iy) in the plane requires only an inversion of a tridiagonal system of size nz (being nz the number of cells in z direction) at each iteration. The velocity field is conveniently updated at each iteration as well and, in return, there's no need to store in memory the entire ϕ scalar field explicitly. Correspondingly, also the pressure field at a given column in z direction is updated during each call to the subroutine.

Finally, flowrate adjustment is performed at the end of the `timestep` subroutine. This is achieved by first computing the difference between the actual and the imposed flowrate; the lack or excess in mean bulk velocity is then consequently ascertained and used to update both the velocity field and the mean pressure gradient needed at the successive time-step to drive the flow. Of course, this operation is not performed for a CPG simulation (*i.e.* at constant pressure gradient).

`iofiles.cpl` collects all the subroutines needed for input and output purposes. Through a `USE` call to `iofiles.cpl` from the main script the initial flow-field is set up. The latter can be either given as an external input or initialized as a laminar flow profile by the program itself.
An output is realized in two different ways using subroutines `savefield` and `output`. The former allows saving the entire flow-field on an external file, while, the latter prints out, on the standard output, simple information about each iteration.

Finally, periodic boundary conditions and parallel execution are made possible by the two files `parallelbcs.cpl` and `parallelbcs.h`. Scheduling and communication between two or more machines are realized through these two files. Nonetheless, they are also needed for serial executions, because subroutines for enforcing periodic boundary conditions are contained in `parallelbcs.cpl`.

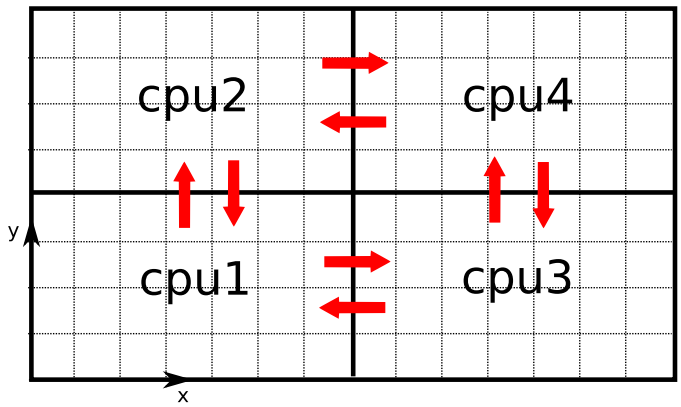

Figure 4.9: *Communication between domain partitions*

4.6 Parallel strategy and scaling performances

In order to reduce execution time as much as possible, the program can be run in parallel between multiple machines. In practice, the computational domain can be partitioned in different pieces by cutting it along the streamwise and spanwise directions. Governing equations are then advanced at each time-step almost independently for all the partitions. This approach is possible and convenient because just few information needs to be shared among separate portions of the domain. Fig.4.9 clarifies this fact; mainly, it is shown a view, in the $x-y$ plane, of a domain divided into four pieces. For each partition, a different machine is assigned, namely cpu1, cpu2, cpu3, and cpu4. Since information is shared only through the boundaries of adjacent domain pieces, it comes clear that cpu1 and cpu4 don't communicate as well as cpu2 and cpu3.
During a given time-step, the update of the flow-field is first performed for the interior of each partition, while, only when surrounding domain portions have all been updated, the boundary is treated. For this purpose, as well as for periodic boundary conditions enforcement, ghost boundaries are employed.

To asses parallel scaling performances and to determine the optimal setup to run the program on a specific architecture, a set of measurements was carried out. Particularly, this was realized on a computational mesh, of size $nx = 400, ny = 350, nz = 250$, chosen according to the required resolution of all the cases tested in the present work. All the measures reported in the following refer to an A2 KNL partition on the Marconi cluster at Cineca laboratories. The key index of scalability performances of a numerical code is the speed-up, which is defined as the ratio of serial to parallel wall-clock times required for the execution of a defined task. Here this is considered to be:

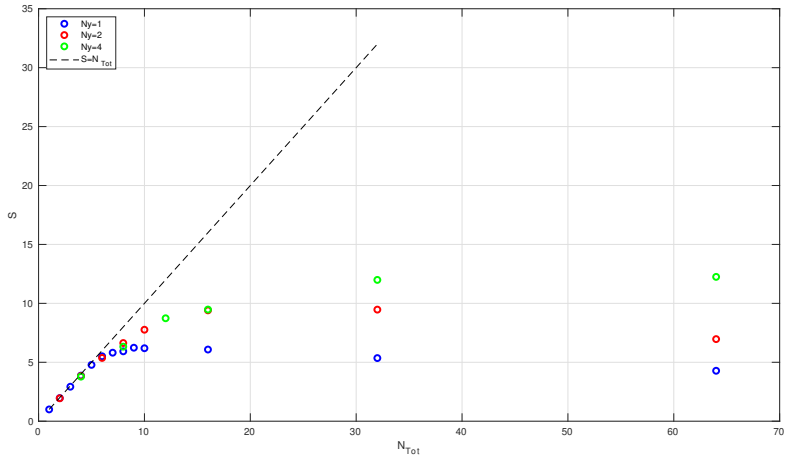

Figure 4.10: *Speed up*

$$S = \frac{\Delta t_s}{\Delta t_p} \tag{4.17}$$

where Δt_s and Δt_p are the times needed for the execution of ten temporal iterations using a serial and a parallel (with p machines) configurations respectively. The ideal characteristic for speed-up would be a linear law, as, in such a case, a parallel run with p machines would imply a time reduction by a factor p with respect to serial execution. The measured speed-up is reported in fig.4.10; it can be noticed that the numerical code has good scaling features only up to a limited number of machines.
Another critical parameter is the efficiency of the scaling, defined as:

$$E = \frac{p}{S} \tag{4.18}$$

again, being p the total number of machines of a configuration and S the corresponding speed-up. For an ideal linear scaling, the efficiency would be equal to one. Fig.4.11 reports the measured efficiency of the code; as expected from the previous plot, efficiency degrades quite rapidly with increasing the number of machines.
Given the previous plots, the optimal configuration for parallel execution should be chosen to have the highest value of speed-up along with the maximum possible efficiency. Considering this, and also taking into account actual execution wall-clock times (reported in fig.4.12), the setup chosen was that deploying $p = 16$ with $Nx = 4$ and $Ny = 4$ (where Nx and Ny are the numbers of machines in streamwise and spanwise directions). This configuration allowed for a speed-up of about 9.5 along with an efficiency of

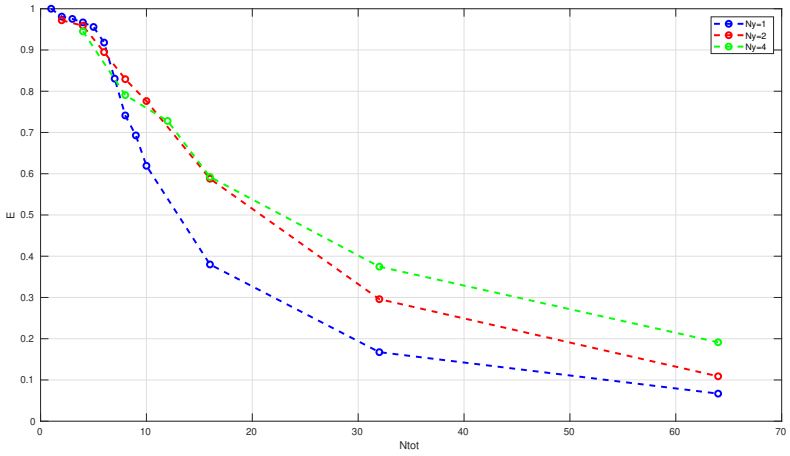

Figure 4.11: *Scaling efficiency*

approximately 60% and a total time per iteration of about 14 seconds.

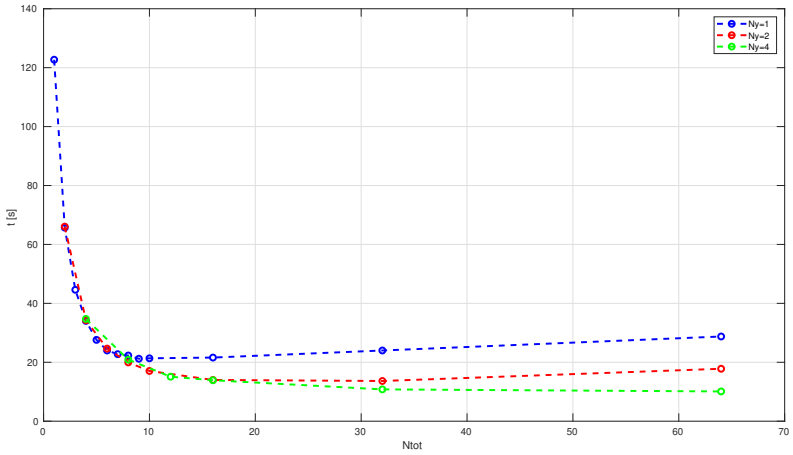

Figure 4.12: *Measured wall-clock time per iteration*

Chapter 5

Numerical experiments definition and results

A series of direct numerical simulations (DNS) were performed in order to assess the adequacy of the numerical method, presented in the previous chapter, of dealing with immersed moving boundaries. To this end, the interesting flow-control strategy, presented by Nakanishi, Mamori and Fukagata in [35], was taken as reference for comparing results obtained with the current immersed boundary numerical technique applied to the same problem. The proposed flow-control methodology aims at reducing the drag in a fully developed channel flow by enforcing a pre-determined wall motion. Particularly, the latter is realized in the form of streamwise-traveling wave trains of wall deformation. More precisely, the two flat walls of a plane channel are perturbed in space with the following time-dependent sinusoidal law:

$$\begin{cases} z_b = -\frac{a}{k\,c} sin\left[k(x-ct)\right] & lower\,wall \\ z_t = 2 + \frac{a}{k\,c} sin\left[k(x-ct)\right] & upper\,wall \end{cases} \tag{5.1}$$

Channel's geometry can be visualized with the help of fig.5.1. No slip boundary conditions that must be enforced at the two walls follow directly from 5.1 and can be written as:

$$\begin{cases} u = 0, \quad v = 0, \quad w = \frac{a}{k\,c} cos\left[k(x-ct)\right] & for\, z = z_b \\ u = 0, \quad v = 0, \quad w = -\frac{a}{k\,c} cos\left[k(x-ct)\right] & for\, z = z_t \end{cases} \tag{5.2}$$

Hence, the flow-control strategy is realized through a combined action of wall deformation and wall-normal velocity enforcement at the solid boundary of the channel. Note that this is different from the control technique of traveling waves of blowing and suction proposed in [31], where only wall-normal velocity is imposed at the two walls of the channel.

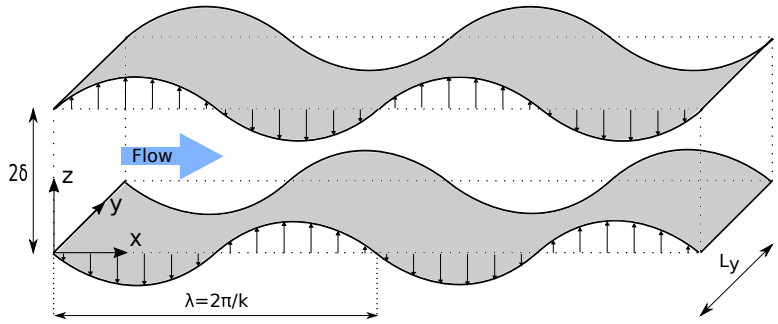

Figure 5.1: *Channel's geometry*

Characterizing parameters of wall actuation are the amplitude of wall velocity a, the wave number k and the phase speed c. Under a certain set of these parameters, it is shown in [35] that such wall motion can be exploited fruitfully for controlling the flow and reducing the total force needed for driving the fluid through the channel. Particularly, with their numerical experiments, they identified two different situations in which drag reduction occurred: the first can be termed as ordinary drag reduction, the second is called relaminarization instead. The former is characterized by a flow that remains turbulent for the whole experiment, while, in the latter, drag reduction is brought about by a transition phenomenon that leads the turbulent flow to reach a laminar state. This feature is of great interest for flow-control purposes as it allows for significant drag reduction rates. In [1] and [12] it is indeed proved that the lowest attainable total power consumption needed for driving and controlling a constant flow rate channel flow is found when the considered flow is laminar. Thus, relaminarization appears as the ultimate goal for drag reduction purposes.
All the simulations carried out in this study aimed at reproducing the phenomena just explained in order to set validation for the current numerical immersed boundary method. To this purpose, a total of eight simulations were performed replicating cases presented in [35] plus a reference plane channel flow needed for comparison.
Setup of numerical experiments and results will be explained in the following of this chapter.

5.1 Numerical experiments definition

The reference geometry considered is that of a plane channel flow with the two walls separated by a distance of $2\delta^*$. Hereafter an asterisk will be used to denote a dimensional quantity. All physical variables are made dimensionless using the mean bulk velocity U_b^* and the half channel-height δ^* and, therefore, the Reynolds number of interest is $Re_b = \frac{U_b^* \delta^*}{\nu^*}$. Here ν^*

represents the kinematic viscosity of the fluid. The (dimensionless) mean bulk velocity is defined as:

$$U_b = \frac{1}{2}\int_0^2 \bar{u}\,\mathrm{d}y. \tag{5.3}$$

where $\bar{u}$ is the mean velocity profile in the channel. As explained in [41], this choice of reference variables is practically convenient for constant-flow rate simulations, and thus the same choice was adopted for this study where all simulations were carried out at a fixed flow-rate.
The sizes adopted for the computational box in the streamwise and spanwise directions are, respectively, $L_x = 4\pi$ and $L_y = 2\pi$; moreover, the flow was assumed to be periodic in these directions. The bulk Reynolds number chosen for the experiments, following what done in [35], was $Re_b = 2800$, corresponding to a friction Reynolds number of $Re_\tau = \frac{u_\tau^* \delta^*}{\nu^*} \approx 180$ with respect to the plane channel case. The friction velocity is defined as $u_\tau^* = \sqrt{\frac{\tau_w^*}{\rho^*}}$, where τ_w^* is the mean total shear stress at the wall and ρ^* is the fluid density. Analogously, it is also defined the viscous lengthscale $\delta_\nu^* = \frac{\nu^*}{u_\tau^*}$. Hereafter, following the usual convention, all physical quantities expressed in viscous units are denoted by a + superscript.
The grid chosen for the simulations was $nx = 400$ (streamwise), $ny = 350$ (spanwise) and $nz = 260$ (wall-normal) with uniform spacing.
Starting from an initial interpolated fully turbulent flow field at the same Reynolds number, all the simulations were run up to reaching 1000 external time units (*e.t.u.*) and sampling was performed every 10 *e.t.u.* in order to guarantee a fair statistical accuracy. An external time unit is here defined according to the current non-dimensionalization convention, *i.e.* $t = t^* \frac{U_b^*}{\delta^*}$.
Each numerical experiment differs from the others by the set of parameters used to determine the control action defined through eq.5.1 and eq.5.2. Tab.5.1 collects the values of control parameters a, k and c for all the simulated cases. In the table are also reported the maximum amplitude of wall deformation $height = \frac{a}{kc}$, the size of the time-step used Δt and the number of the corresponding case found in [35]. Before proceeding with the exposition of computed results, a final remark on the size of the time-steps used is due. As explained in the previous chapter, the employed immersed boundary method suffers from spurious oscillations of computed fluid-dynamic variables arising from a violation of volume conservation when an arbitrary boundary motion is enforced. A remedy to this issue was found for the particular wall motion employed in this study; namely, this reduces to the simple condition 4.16 that merely sets a constraint on the time-step size once that streamwise spacing Δx and wall phase-speed c are assigned. The condition is here reported for clarity:

$$\frac{c\Delta t}{\Delta x} = 1 \tag{5.4}$$

Case	a	k	c	Max wall height	Δt	Corresponding case in [35]
ref.	0	0	0	0	0.03142	”
01	0.3	2	2	0.075	0.01571	8
02	0.3	4	2	0.0375	0.01571	9
03	0.4	2	2	0.1	0.01571	11
04	0.2	1	2	0.1	0.01571	4
05	0.2	2	2	0.05	0.03142	5
06	0.2	4	2	0.025	0.03142	6
07	0.3	1	2	0.15	0.01571	7

Table 5.1: *Wall actuation parameters*

Since the grid size was fixed for all simulations, the time-step needed for each case was computed using the above relation (values can be found in tab.5.1). With this choice, neither oscillations nor numerical instabilities were observed.

5.2 Averaging

Computation of mean flow properties is usually performed using suitable averaging operators that should be chosen according to the geometric characteristics of the considered flow. For a plane channel, a space average can intuitively be defined thanks to the two homogeneous directions (spanwise y and streamwise x); more specifically, considering a generic flow variable $q(x, y, z, t)$, space averaging can be performed through:

$$q_{xy}(z,t) = \frac{1}{L_x L_y} \int_0^{L_x} \int_0^{L_y} q(x,y,z,t)\, \mathrm{d}x\mathrm{d}y \tag{5.5}$$

The quantity q_{xy}, which depends on wall-normal coordinate z and time, can be further averaged in time by using the following definition:

$$\overline{q}(z) = \lim_{T\to\infty} \frac{1}{T} \int_0^T q_{xy}(z,t)\, \mathrm{d}t \tag{5.6}$$

Hereafter, if not otherwise specified, an overbar will be used to denote a quantity averaged both in the $x-y$ plane and time. The two averages thus defined lead to the well-known Reynolds decomposition of the flow-field, namely:

$$q(x,y,z,t) = \overline{q}(z) + q'(x,y,z,t) \tag{5.7}$$

where $q'(x, y, z, t)$ denotes the turbulent random fluctuation.
A different situation is encountered when a flow, confined by two streamwise-periodic wavy walls (as those defined by 5.1), is considered, for the streamwise direction is not homogeneous anymore. On the other hand, standard

averaging can still be performed in the spanwise direction. This is exactly the case faced in the present study, where the channel walls are defined by 5.1. In such a case, following [43], a given quantity can be split into a three-components decomposition as:

$$q(x,y,z,t) = \overline{q}(z) + \tilde{q}(\phi(x,t),z) + q''(x,y,z,t) \tag{5.8}$$

where $\tilde{q}$ and q'' are the periodic and random components respectively. The former is a function of the wall phase $\phi(x,t) = k(x-ct)$, while the latter is a random perturbation of turbulent nature. Collecting these two contributions into the turbulent fluctuation q', the usual two-components decomposition can be recast:

$$\begin{cases} q(x,y,z,t) = \overline{q}(z) + q'(x,y,z,t) \\ q'(x,y,z,t) = \tilde{q}(\phi(x,t),z) + q'' \end{cases} \tag{5.9}$$

According to [43], another space averaging operator, called phase average, can be defined as follows:

$$\langle q\,(x,t)\rangle = \lim_{N\to\infty} \frac{1}{N} \sum_{n=0}^{N} q(\phi + n\lambda, z) \tag{5.10}$$

here λ represents the wavelength of the wavy wall. The symbol $\langle\cdot\rangle$ will be used in the following to denote phase-averaged quantities.
Applying 5.10 to 5.8 it can be shown that a phase-averaged quantity, at a given z coordinate and time instant t, consists of a constant part plus a periodic contribution induced by the wavy wall. More precisely:

$$\langle q(x,y,z,t)\rangle = \overline{q}(z) + \tilde{q}(\phi(x,t),z) \tag{5.11}$$

Hence, the following decomposition of the flow-field naturally arises:

$$q(x,y,z,t) = \langle q(\phi(x,t),z)\rangle + q''(x,y,z,t) \tag{5.12}$$

Averaging operators and flow decompositions just explained will be used throughout the chapter for studying mean-flow properties of all the controlled cases, similarly to what done in [35], [47] for streamwise-traveling wall deformation waves, [30] in the context of blowing-and suction waves and [4] [17] for flows over stationary wavy walls.

5.3 Reference case

Results regarding the plane channel flow are discussed first. This case is of great importance as it sets a reference with which the behavior of the flow, observed in all other simulations, can be compared.
A comparison of the computed viscous units with those established by Kim, Moin and Moser for the same flow in their famous paper [22] is reported in

	Re_τ	u_τ	δ_ν	U_b^+
Present	177.032	0.06323	0.005649	15.82
Kim et al.	178.12	0.06398	0.005614	15.63

Table 5.2: *Computed viscous units*

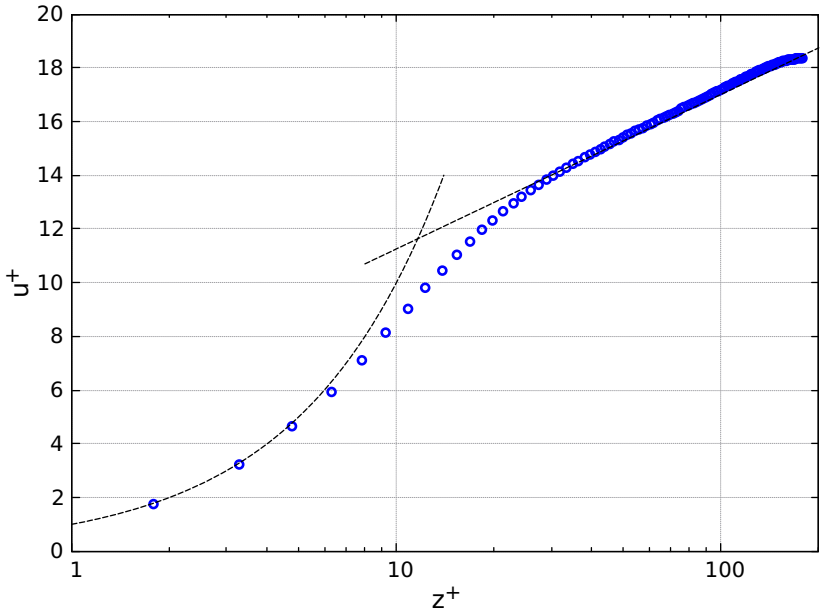

Figure 5.2: *Mean velocity profiles:* ○, *computed mean-velocity*; - - - - -, *law of the wall*

tab.5.2. From the table a little discrepancy between computed and reference viscous units can be observed; the cause may be addressed to the different numerical approach used (in [22] a spectral method was adopted), along with differences in grid resolution; yet, the results obtained were considered satisfying for the purpose of the present study. Using the computed value of the viscous length δ_ν, the grid resolution in wall units is found to be: $\Delta x^+ \approx 5.6$, $\Delta y^+ \approx 3.2$ and $\Delta z^+ \approx 1.5$.
Mean flow field properties are obtained by applying the averaging both in space and in time using eq.5.5 and eq.5.6. Computed mean flow quantities will be now presented.
Fig 5.2 is a semi-logarithmic plot of the mean streamwise velocity profile as a function of the distance from the lower wall. Velocity is normalized by the friction velocity u_{tau} and the wall-normal coordinate z is expressed in wall units; only the lower half of the velocity profile is represented in the figure. On the same plot it is also drawn the classical law of the wall for the viscous sub-layer and the logarithmic region. More precisely, these are defined by

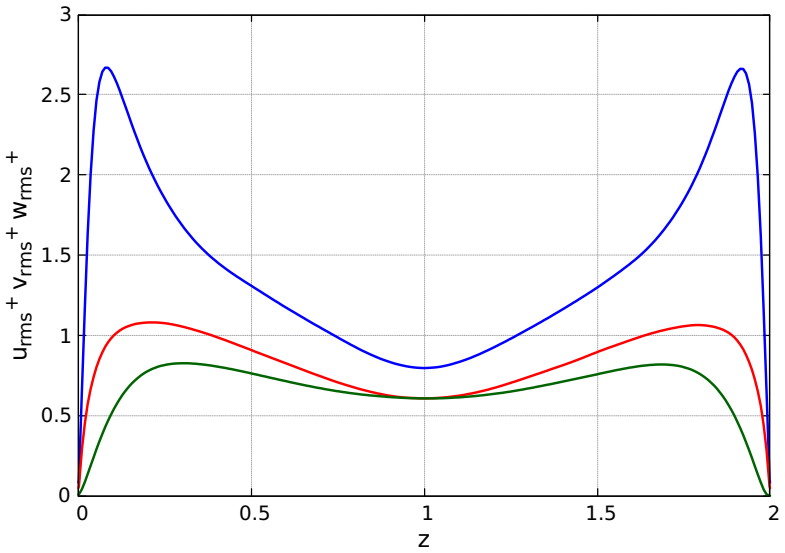

Figure 5.3: *Turbulence intensities:* ——, u^+_{rms}; ——, v^+_{rms}; ——, w^+_{rms}

the analytical expressions:

$$\begin{cases} u^+ = z^+ & viscous\,sublayer \\ u^+ = \frac{1}{K} log\, z^+ + A & log\ region \end{cases}$$

where the values of the Von Karmann constant K and A are set according to [22]: $\frac{1}{K} = 2.5$, $A = 5.5$. The computed velocity profile exhibits a visible logarithmic region for $z^+ > 30$ whose slope is largely in agreement with that suggested in [22]. A small discrepancy is however evidenced in the magnitude of the velocity in the same region, while conformity is found in the viscous sub-layer ($z^+ < 6$) between the computed profile and the analytical curve.

Root-mean-square ($r.m.s.$) turbulence intensities u_{rms}, v_{rms} and w_{rms}, normalized by the friction velocity u_τ, are reported in fig.5.3 as function of the distance from the lower wall. Profiles found are symmetric with respect to the channel centerline, indicating that sampling was sufficient to assure a good statistical accuracy. Expressed in wall units, the location of the peak of the streamwise turbulence velocity fluctuation u_{rms} is found at $z^+ \approx 13$ and its value is $u_{rms} \approx 2.6$, a result which is in accordance with the expectations.

The Reynolds shear stress $-\overline{u'w'}$ is represented in fig.5.11; the symmetry of the curve with respect to the centerline and an accentuated linear behavior in the middle region of the channel can be appreciated and are symptoms of the statistical equilibrium of the flow.

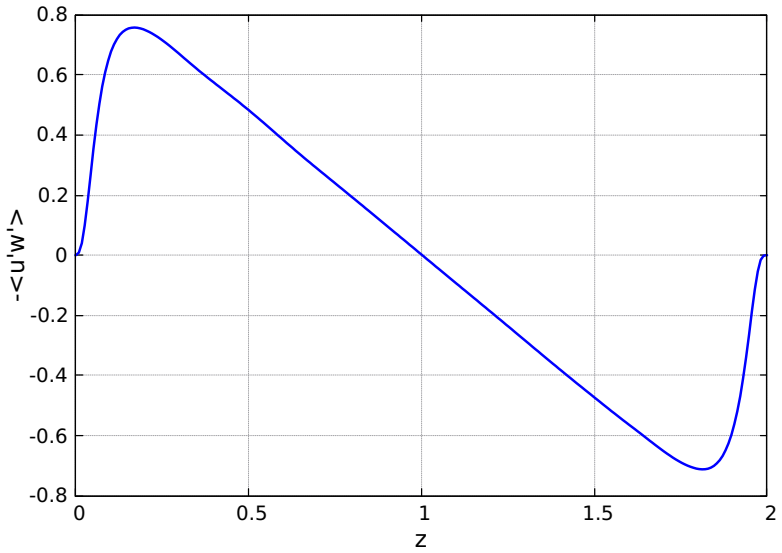

Figure 5.4: *Reynolds shear stress* $-\overline{u'w'}$

Even though small discrepancies were observed between the computed reference plane case and results presented in [22], this simulation was still considered satisfying for the purpose of the present study.

5.4 Relaminarization

Relaminarization was observed with three different cases, namely *case* 01, *case* 02 and *case* 03 (see tab.5.1 for actuation parameters). These correspond to cases 8, 9 and 11 of Fukagata *et al.* where relaminarization occourred as well.

The first figure presented here, fig.5.5, shows the time trace of the turbulent kinetik energy $\frac{1}{2}\left(\langle u'u'\rangle + \langle v'v'\rangle + \langle w'w'\rangle\right)$ for cases 01, 02, 03 and for the reference plane channel flow. As can be expected, the transition from turbulence is never-quite-attained completely, as it is seen from the figure that the turbulent kinetic energy ($t.k.e$) tends asymptotically to zero without never vanishing completely. Nonetheless, in practice, an arbitrary threshold can be considered and the flow may be said "fully laminar" once that the $t.k.e.$ reaches values smaller than that threshold. For instance, in the present study, it was found that, at $t \approx 350\, e.t.u.$, the $t.k.e.$ of all relaminarization cases was already three orders of magnitude less than that of the plane reference case. Of course, this is just an operational convention employed to make a practical distinction between turbulent and laminar flows.

The turbulent to laminar transition of the flow can be visualized with the help of fig.5.6, which depicts some flow field visualizations for the representative relaminarization *case* 03. Namely, on the left column (figures b, d

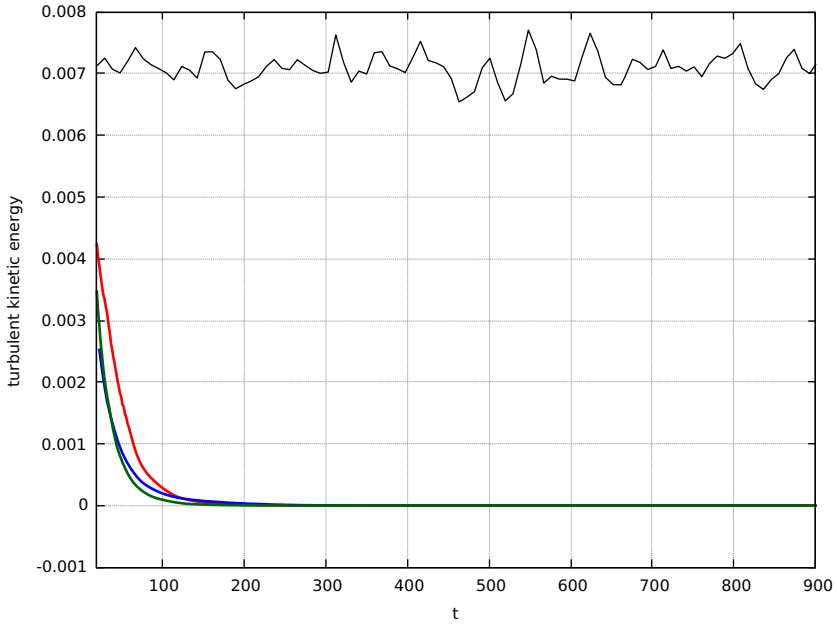

Figure 5.5: *Time trace of the mean turbulent kinetic energy:* ——, *flat walls*; ——, *case* 01; ——, *case* 02; ——, *case* 03

and f), instantaneous color contours of the streamwise velocity component at different time instants are represented at the cross section of the channel where the phase $\phi = k(x - ct)$ of the wall is zero. This location corresponds to the position where wall velocity is maximum. These figures should be compared to the representative flow-field in the cross section of the channel for the plane reference case in fig.5.6a. On the other hand, on the right column (figures c, e and f), computed mean velocity profiles, for both plane channel and *case* 03, are compared with each other and with the laminar Poiseuille profile at different streamwise locations and at different time instants. Color contours in the figures represent the instantaneous Reynolds shear stress distribution $-u'w'$ in the channel.

For the plane channel, fig.5.6a shows vortical structures in the entire flow field, especially in the close vicinity of the walls where these structures assume a typical streaky shape. A similar vortical arrangement, even though somewhat weakened, can also be observed in fig.5.6b, which represents the flow at an early stage of the relaminarization process ($t = 23$). It can be noticed a clear vertical alignment of the velocity in the proximity of the walls induced by actuation; in that region, the fluid is pumped away from the walls and vortical structures seem to be pushed away as well. Following the evolution of the flow, at $t = 157$ (fig.5.6d) there appears to be a highly ordered pattern of the velocity close to the walls and no signs of large vortical structures are visible in that region. Nonetheless, some irregularities

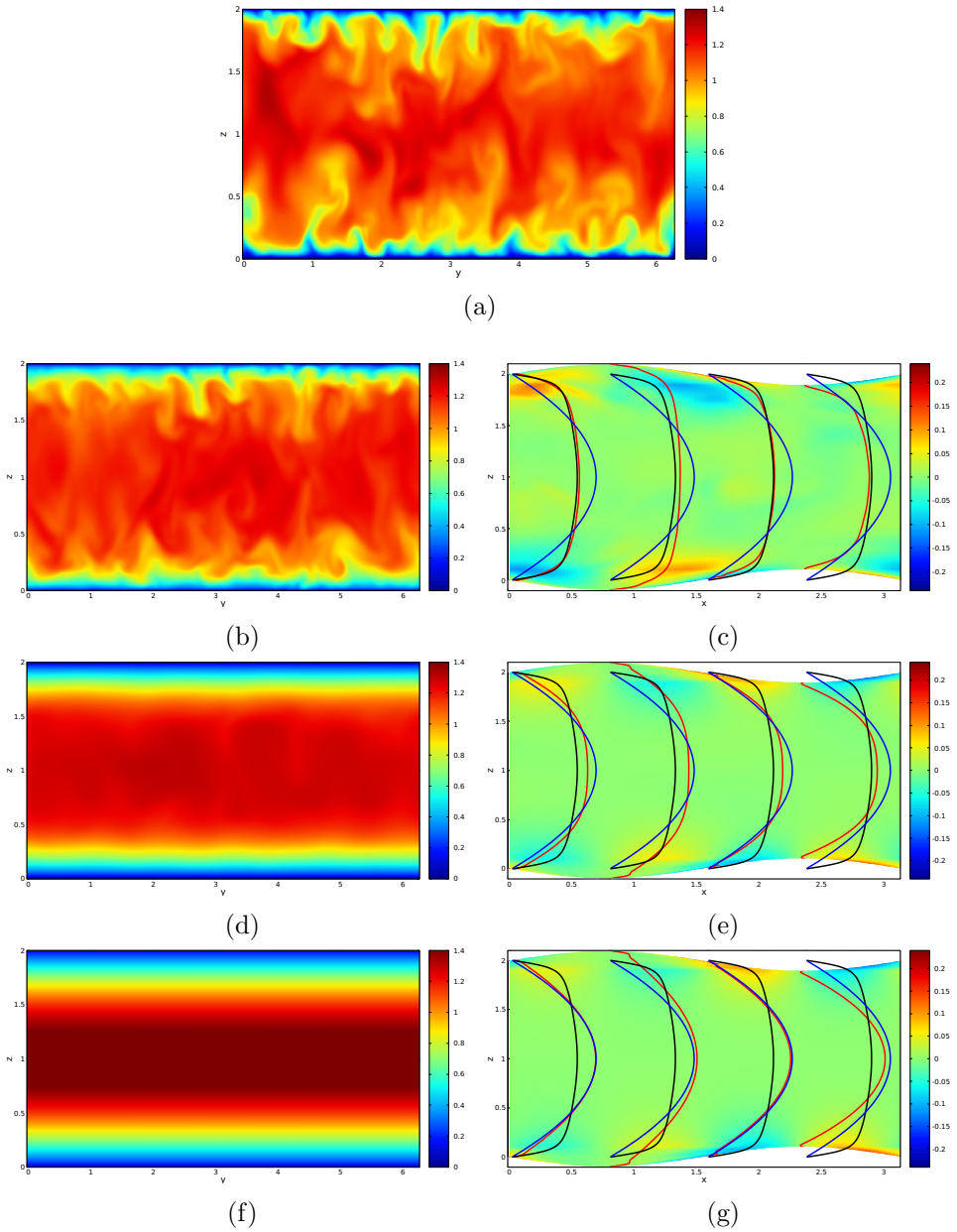

Figure 5.6: *Flow visualization for case* 03. *Left column: color contours of the streamwise velocity component in the* $y-z$ *plane at* $\phi = 0$*; (a), plane channel; (b),* $t = 23$*; (d),* $t = 157$*; (f),* $t = 628$*. Right column: mean velocity profiles at different streamwise locations:* ———*, case 03;* ———*, plane channel;* ———*, laminar Poiseuille; color contours represent istantaneous Reynolds shear stress* $-u'w'$ *at time instants (c),* $t = 23$*; (e), t=157; (f), t=628*

can still be observed in the central area of the channel. After a sufficiently long time, also these residual irregularities eventually disappear everywhere, leaving a perfectly ordered flow that may be termed as laminar. This situation is depicted in fig.5.6f for the flow field at $t = 628$.
From figures on the right column of fig.5.6, it can be noticed that wall actuation has a significant impact on Reynolds shear stress, especially close to the walls, where its distribution displays a regular pattern that becomes more evident as time evolves. Boundary motion induces the Reynolds shear stress distribution to peak in the proximity of the walls and to have a very small magnitude elsewhere. The highly regular pattern in the Reynolds stress distribution close to the walls is clearly visible observing the flow field at a later stage of the relaminarization process, for instance at $t = 628$ in fig.5.6g.
Starting from fig.5.6c, which refers to the flow-field at $t = 23$, mean velocity profiles at different streamwise locations closely resemble the mean velocity profile of the reference case, in that they all are characterized by a flattened shape and a steep gradient close to the walls. On the other hand, a more rounded profile can be observed at time $t = 157$ in fig.5.6e. As the relaminarization process takes place, mean velocity profiles tend to become very similar in shape to the laminar Poiseuille profile (*i.e.* a parabola). This is evident at time $t = 628$ (fig.5.6g), where computed and analytical laminar profiles seem to match closely in the central region of the channel, whereas, close to the walls, differences in shape are apparent. Some reverse flow can also be noticed in the proximity of the crests of the walls. As explained in [16], this phenomenon is due to the boundary movement that is responsible for carrying fluid particles around in closed loop tracks. Observing mean velocity profiles, it can also be pointed out that flow-rate is not conserved locally, as it is apparent that it varies at different streamwise locations. However, the flow-rate averaged in the entire channel was enforced to be constant at each time instant by the numerical strategy.

The evolution of the mean flow profile at different streamwise locations is also reported for *case* 01 in fig.5.7. The three figures refer to time instants $t = 23$, $t = 157$ and $t = 628$. Profiles of the uncontrolled case and the laminar channel are also reported for comparison. Similar observations to *case* 03 hold; it is evident how the relamnarization process modifies the mean velocity from a flattened curve to a rounded profile that closely matches the Poiseuille profile.

For *case* 01 fig.5.8 reports the color contours of the turbulent kinetic energy ($t.k.e.$) at time instants $t = 23$, $t = 157$ and $t = 628$. Note that the range of the colorbar is adapted in each figure. Initially, at $t = 23$, the $t.k.e$ is more intense in the near-wall region, especially in the trough of the wave. As time passes, at $t = 157$, the peak of the $t.k.e.$ is reduced in intensity and it is shifted toward the central region of the channel. Later, at $t = 628$, the $t.k.e.$ has an extremely low magnitude everywhere in the channel. Peaks of

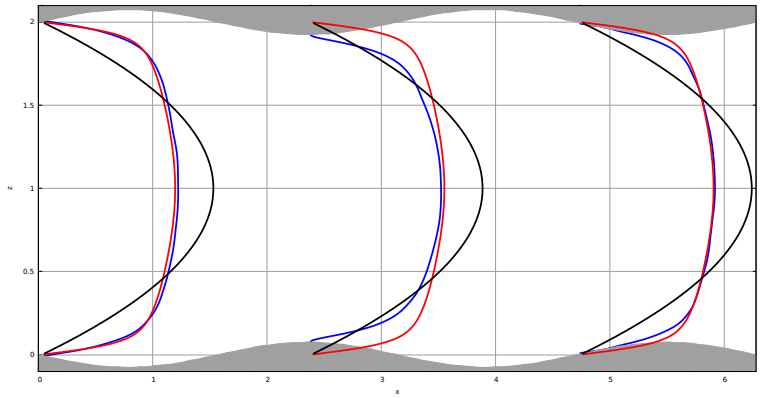

(a)

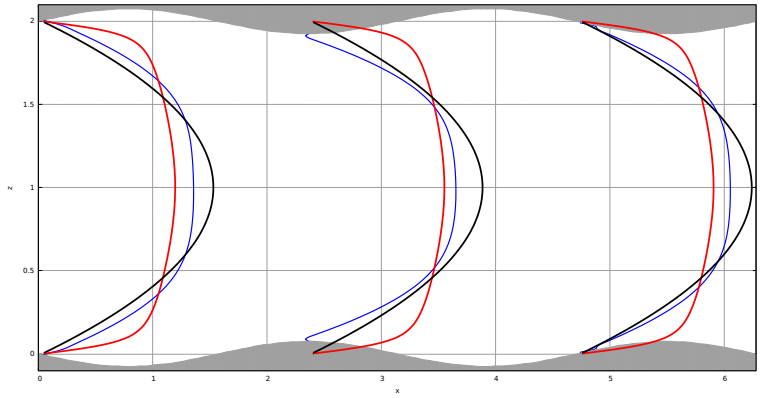

(b)

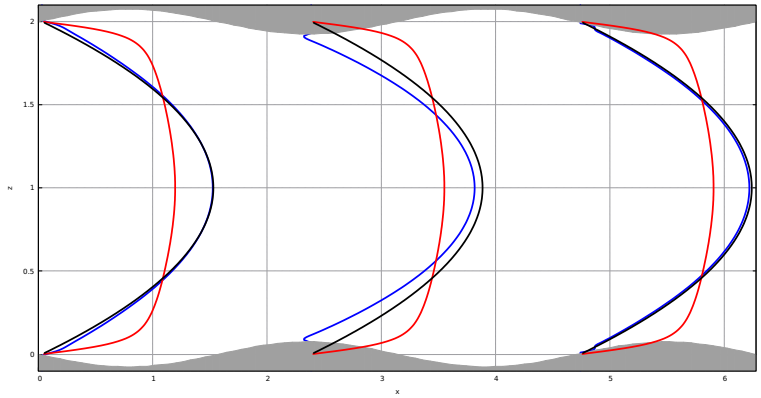

(c)

Figure 5.7: *Mean velocity profiles at different streamwise locations for case* 01. *(a),* $t = 23$*; (b), t=157; (c), t=628*

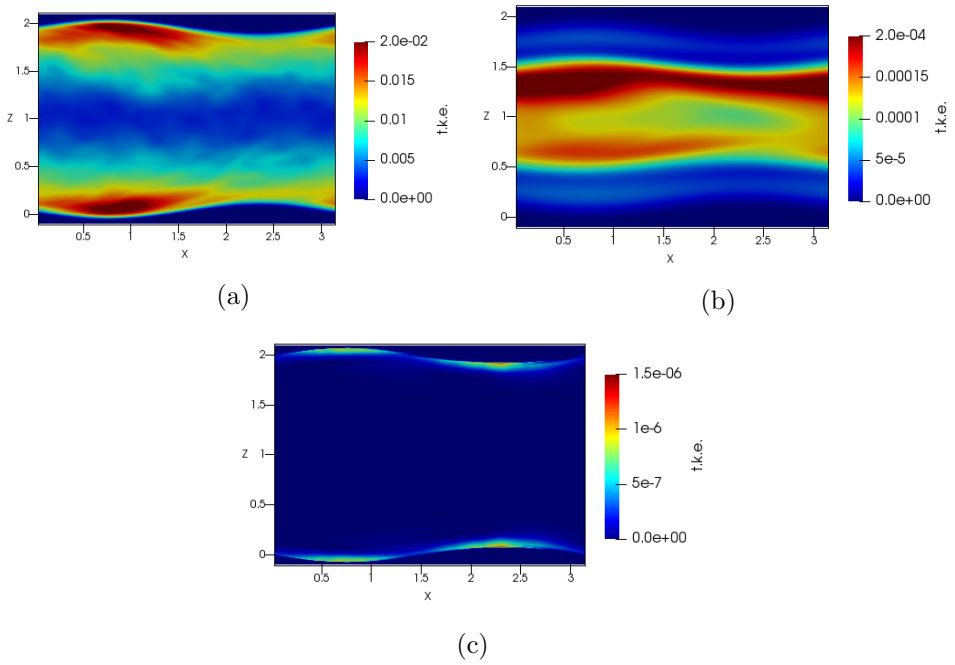

Figure 5.8: *Color contours of the turbulent kinetic energy for case* 01. *(a), t = 23; (b), t=157; (c), t=628*

small magnitude are found in the close proximity of the two walls.

5.5 Fully turbulent cases

With the term ordinary drag reduction, authors of [35] referred to cases in which drag reduction, with respect to the plane reference case, was achieved, but no relaminarization effects were observed. The same was found in the present study for *case* 04, *case* 05, *case* 06 and *case* 07 (which correspond to cases 4, 5, 6, 7 in [35]).
Fig.5.9 represents mean velocity profiles of *case* 04, obtained by application of the phase and time averages (eq.5.10 and eq.5.6), at different streamwise locations. In the figure it is also reported the mean velocity profile for the reference plane case for comparison. As it can be noticed, computed profiles have a characteristic flattened shape, suggesting that the flow remains turbulent for the entire simulation. Differently from *case* 03 (fig.5.6), here no evident reverse flow is visible, despite the fact that both cases share the same wall deformation amplitude (see tab.5.1)). Conversely, also in this case, the local flow-rate is seen to vary along the channel, as it is clear in the figure that different mean-velocity profiles have a different area.

Exploiting the phase average defined in eq.5.10, the flow field can be

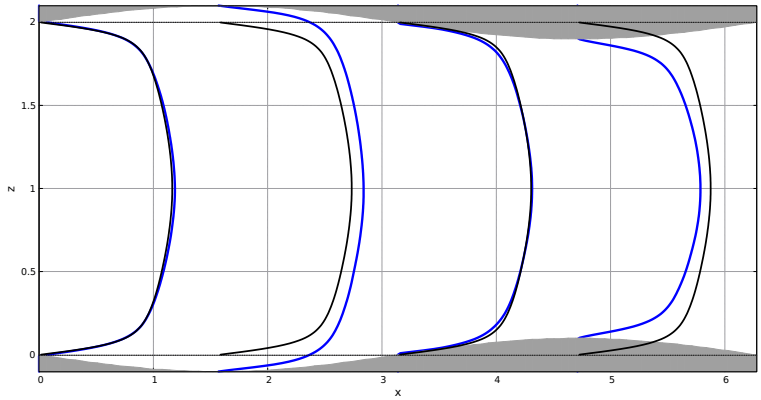

Figure 5.9: *Mean velocity profiles at different streamwise locations:* ——, *case 04;* ——, *plane channel*

decomposed using eq.5.12, namely:

$$\mathbf{u}(x,y,z,t) = \langle \mathbf{u}(\phi,z) \rangle + \mathbf{u}''(x,y,z,t) \tag{5.13}$$

where, again, $\phi = k(x - ct)$ is the phase of the wave and $\mathbf{u}''$ is the turbulent random fluctuation.

Root-mean-square turbulence intensities profiles, normalized by the mean bulk velocity, are plotted in fig.5.10 for *case* 04 (left column, figures: a, c, e and g) and *case* 06 (right column, figures: b, d, e, f and h). Each figure corresponds to a different location along the streamwise direction of the channel. In each plot, *r.m.s.* turbulent velocity fluctuations of the reference plane channel flow are also reported for comparison. Mainly, as it can be noticed, actuation has a visible effect on turbulence fluctuations in the region close to the channel's wall. However, different behaviors are evidenced at different stations along the channel. Broadly speaking, for *case* 04, turbulence intensities appear weakened at $\phi = 0$ (5.10a), where wall velocity is maximum, and at $\phi = \frac{3}{2}\pi$ (5.10g), which corresponds to the crest of the wave, where wall velocity is zero. On the other hand, little no effect is visible at $\phi = \pi$ (5.10e), where wall velocity is minimum, while, at $\frac{\pi}{2}$ (*i.e.* at the trough of the wave, 5.10c), a slight increase in the peak of the streamwise turbulent velocity fluctuation is found.

The presence of the wall has the intuitive effect of shifting profiles away from the mean wave axis $z = 0$; as a consequence, also peaks of turbulence intensities result shifted accordingly. Differently from *case* 04, it is now observed that wall actuation has a visible weakening effect, close to the wall, on turbulence intensities at all streamwise locations for *case* 06 (right column figures in 5.10). Thus, wall motion of *case* 06 appears to be more capable of weakening turbulence, if compared to actuation of *case* 04. Random Reynolds shear stress $-\langle \overline{u''w''} \rangle$ (RSS) profiles, normalized by the squared

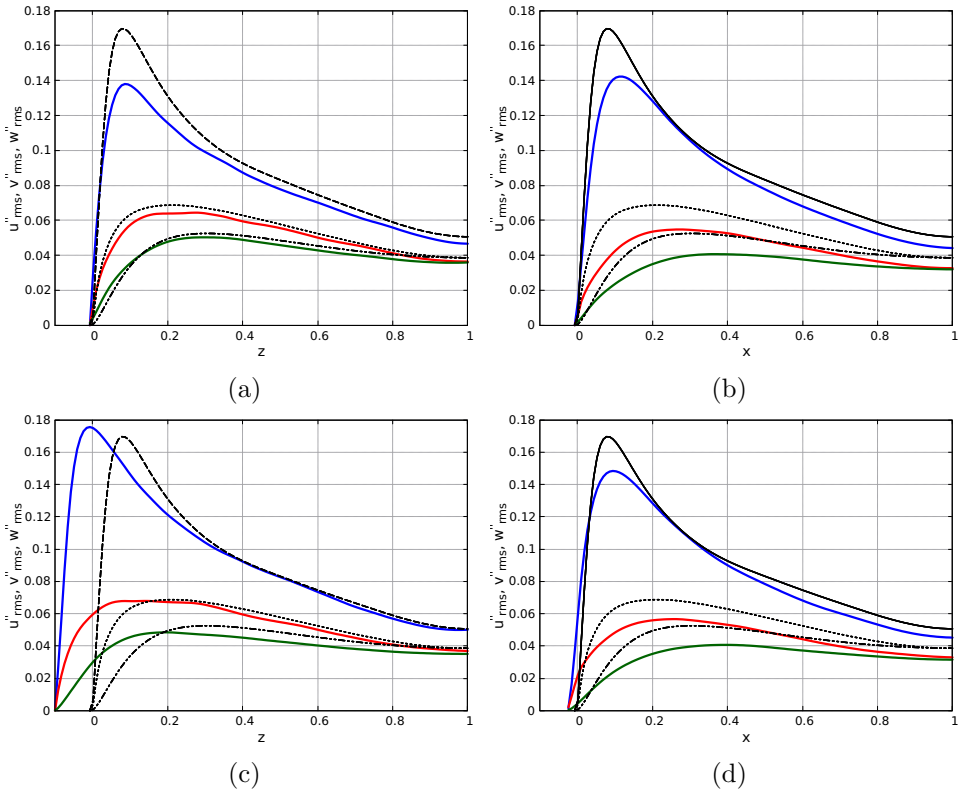
0.18
0.16
0.14
0.12
0.1
0.08
0.06
0.04
0.02
0
0.2
0.4
0.6
0.8
1
z
x
u''rms, v''rms, w''rms

(a) (b)

(c) (d)

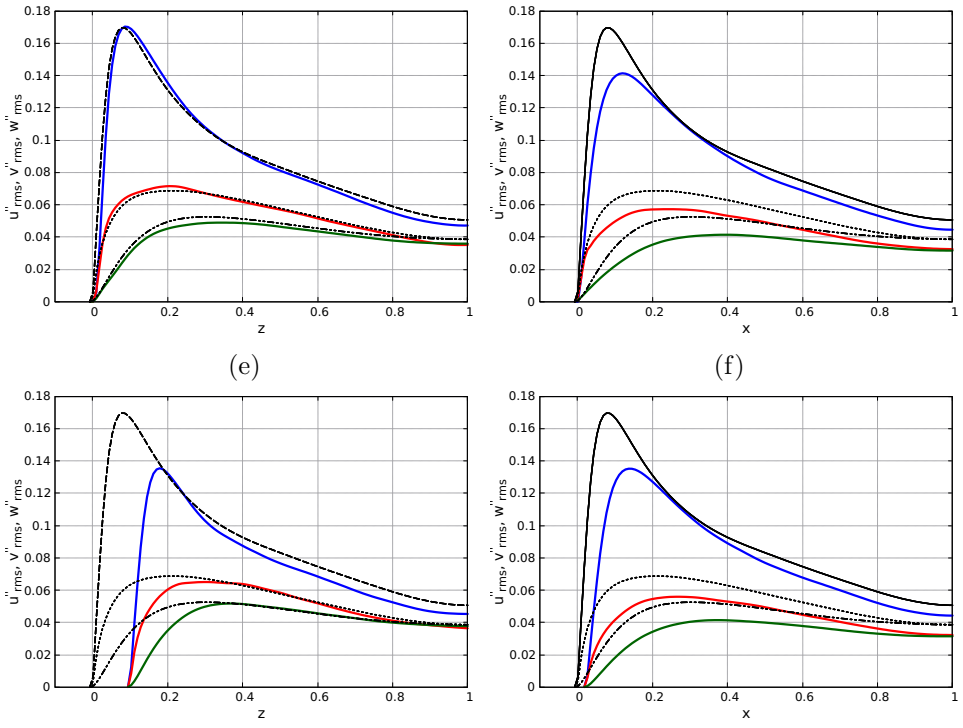

Figure 5.10: *Root-mean-square turbulent velocity fluctuations at different streamwise locations for case* 04 *(left column) and case* 06 *(right column). Case 04 and Case 06:* ——, u_{rms}; ——, v_{rms}; ——, w_{rms}. *Plane channel:* - - - - -, u_{rms}; ·····, v_{rms}; -·-·-·, w_{rms}

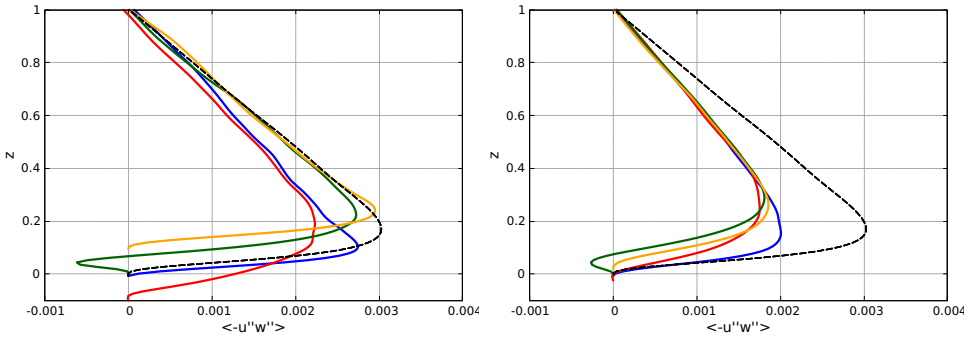

Figure 5.11: *Random Reynolds shear stress profiles for case* 04 *(left) and case* 06 *(right).* ——, $\phi = 0$; ——, $\phi = \frac{\pi}{2}$; ——, $\phi = \pi$; ——, $\phi = \frac{3}{2}\pi$; - - - - -, *plane channel*

mean bulk velocity, are depicted in fig.5.11 for both *case* 04 (a) and *case* 06.

In each figure, a dashed line represents RSS ($-\overline{u'w'}$) for the reference case, while solid lines of different colors correspond to RSS profiles at different locations (namely, $\phi = 0$, $\phi = \frac{\pi}{2}$, $\phi = \pi$ and $\phi = \frac{3}{2}\pi$). Comparing the two images, it is evident how wall actuation of *case* 06 is more capable of reducing random RSS (with respect to the reference case) at all different phases of the wall. In fact, a tangible RSS reduction is only evident in *case* 04 at $\phi = 0$ and $\phi = \frac{\pi}{2}$. However, what is remarkable in both cases is that a negative RSS is observed close to the wall at $\phi = \pi$. The very same phenomenon is also reported in the reference paper [35], where it is stressed out the importance of this occurrence on the drag reduction mechanism. Their argument stands on the solid basis that the skin friction coefficient in a fully developed turbulent channel can be written as:

$$C_F = \frac{6}{Re_b} + 6\int_0^1 (1-z)(-\overline{u'w'})\,\mathrm{d}z \tag{5.14}$$

This identity comes from the integration of the Navier-Stokes equations and its derivation can be found in [9] and [2]. Notably, eq.5.14 states that the skin friction coefficient in a turbulent channel equals that of a laminar channel plus a contribution which is exclusively due to turbulence. The latter is, as a matter of fact, a weighted average of the mean RSS in the channel in which the weight is represented by the distance from the wall. Thus, occurrences of locally negative RSS have an intuitive beneficial effect in reducing the skin friction drag coefficient, especially when they appear in a region close to the channel's wall. Note also the strong implication of eq.5.14: if the second term on the right-hand side of the equation could be made negative, the drag in the channel would achieve a sub-laminar value. This assertion

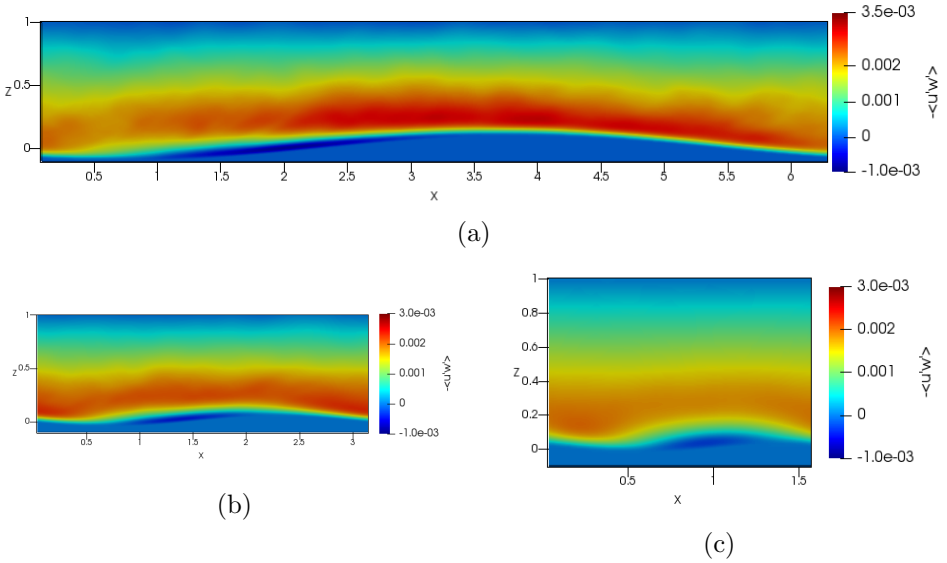

Figure 5.12: *Random Reynolds shear stress color contours. (a), case* 04*; (b), case* 05*; (c), case* 06

was indeed proved to be correct in [31], where sub-laminar drag was attained employing traveling waves of blowing and suction. Hence, confidence that the same result can also be achieved with the present control strategy is tangible. However, it must be recalled that, as mathematically proved in [12] and [1], laminar flow sets a lower bound on the total power required to drive the flow which cannot be surpassed even when a sub-laminar drag is attained in the channel.
Fig.5.12 represents color contours of random RSS in the $x-z$ plane (at fixed $y = \pi$) for *case* 04, *case* 05 and *case* 06. All the figures represent only the lowe half of the channel. Even though the fluid-solid interface is not easily distinguishable, thin regions of negative RSS in the near-wall region are observed in all the figures. Similar findings were also observed for all other cases, providing good evidence of the positive effect of streamwise travelling waves in promoting the appearance of near-wall negative RSS.

5.6 Drag reduction

The ultimate goal of applying a control action, such as that presented by far, is that of achieving drag reduction with respect to a reference configuration. Hence, it arises the necessity of defining a suitable index capable of providing an actual measure of the drag reduction performance.
First, a distinction between different sources of drag should be taken into account; in a plane channel flow driven at constant flow-rate, the only source

of drag is that due to friction at the two walls of the channel.
A natural index, usually employed, is the friction drag coefficient defined, according to the current choice of reference variables, as:

$$C_f = \frac{\tau_w^*}{\frac{1}{2}\rho^* U_b^{2*}} = \frac{2}{Re_b}\frac{\mathrm{d}\bar{u}}{\mathrm{d}z} \tag{5.15}$$

where τ_w^* is the friction shear stress at the wall and ρ^* and μ^* are, respectively, the density and the viscosity coefficient of the fluid. It is recalled that all dimensional quantities are denoted with an asterisk.
On the other hand, when a channel flow confined by wavy or, more generally, rough walls is of concern, also pressure drag must be accounted for. Thus, it is legitimate to define the total drag coefficient C_D as made up of two contributions, namely:

$$C_D = C_f + C_{DP} \tag{5.16}$$

where C_f is the skin friction drag coefficient, due to the viscous shear stress at the wall, and C_{DP} is the pressure drag coefficient. As reported in [34], these two terms can be defined by:

$$\begin{cases} C_f = \frac{1}{\frac{1}{2}\rho^* U_b^{2*}} \int_S (\boldsymbol{\tau}\mathbf{n}) \cdot \mathbf{e}_1 \mathrm{d}S \\ C_{DP} = \frac{1}{\frac{1}{2}\rho^* U_b^{2*}} \int_S (-p\mathbf{n}) \cdot \mathbf{e}_1 \mathrm{d}S \end{cases}$$

where $\boldsymbol{\tau}$ is the viscous stress tensor, $\mathbf{e}_1$ is the streamwise unit vector, and $\mathbf{n}$ is the unit normal vector to the channel's boundary surface S.
In the present study, a slightly different parameter has been employed for measuring and comparing drag performances of different controlled flows. In particular, the mean pressure gradient, adjusted at each time-step to drive the flow at a constant rate, was used to measure the total drag felt by the flow. As stated in [19], the mean pressure gradient that is needed to pump the flow at a fixed volume rate is defined as the total drag force acting on the fluid divided by the channel's volume.
Even though the relation with the total drag coefficient is straightforward, its computation was not performed in this work.
Fig.5.13 presents the runtime-measured time traces of the mean pressure gradient found for all the controlled cases along with that of the plane reference case. In the same figure, it is also showed the theoretical laminar value computed from the exact solution of the Poiseuille plane channel. More precisely, the latter is found to be:

$$-\overline{\frac{\mathrm{d}P}{\mathrm{d}x}} = \frac{3}{Re_b} = 1.0714 \cdot 10^{-3} \tag{5.17}$$

Namely, in the figure, two different behaviors are distinguished. It is clear

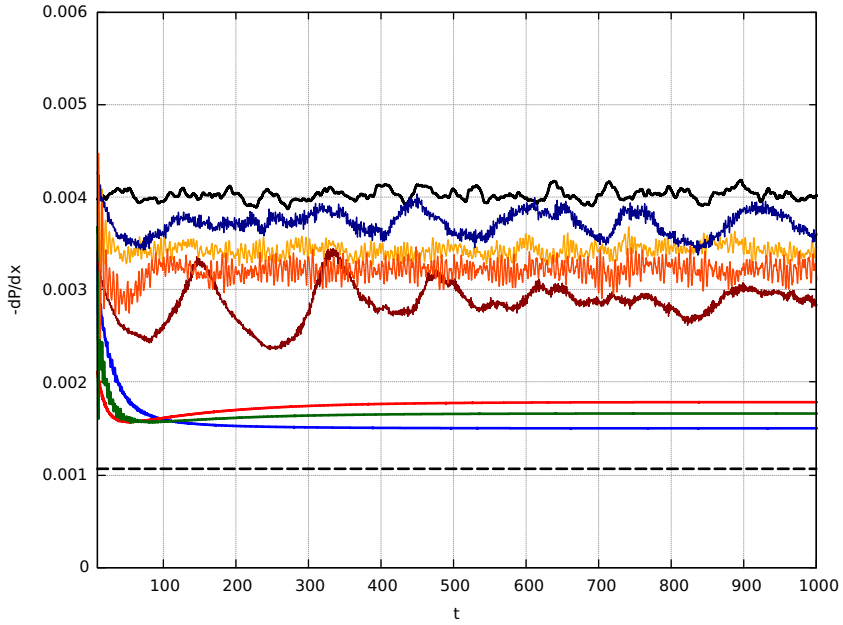

Figure 5.13: *Time traces of the mean stramwise pressure gradient:* ——, $reference$; ——, *case* 01; ——, *case* 02; ——, *case* 03; ——, *case* 04; ——, *case* 05; ——, *case* 06; ——, *case* 07; - - - - -, $laminarPoiseuille$

that in *case* 04, *case* 05, *case* 06 and *case* 07, drag reduction is achieved at the statistical steady state, for the average measured value of the mean pressure gradient is less than that corresponding to the uncontrolled channel; however, the flow remains turbulent for the entire time of the simulation, as already discussed in the preceding section of this chapter. Signs of turbulence are also evident in the time-trace of the mean pressure gradient, which is made up of a mean value plus unpredictable turbulent fluctuations.
On the other hand, *case* 01, *case* 02 and *case* 03 display an easily distinguishable behavior, if compared to other curves in the figure. With these cases relaminarization was indeed observed and, as it can be noticed, the trace of the pressure gradient appears as a smooth curve. A significant reduction in the required pumping force per unit volume (*i.e.* the mean pressure gradient) is achieved for all three relaminarization cases, but a considerable distance from the limiting laminar value is still seen. This difference might be explained by two arguments: first, the curved shape of the wavy walls produces a pressure drag; second, the pumping effect induced by the peristaltic motion of the walls is hidden inside the measured value of the pressure gradient. This is caused by the procedure by which the volume force, needed to pump the flow, is computed during the simulation. As a consequence, the mean pressure gradient reported in fig.5.13 is made up of two contributions: the external pressure jump, actually required to drive

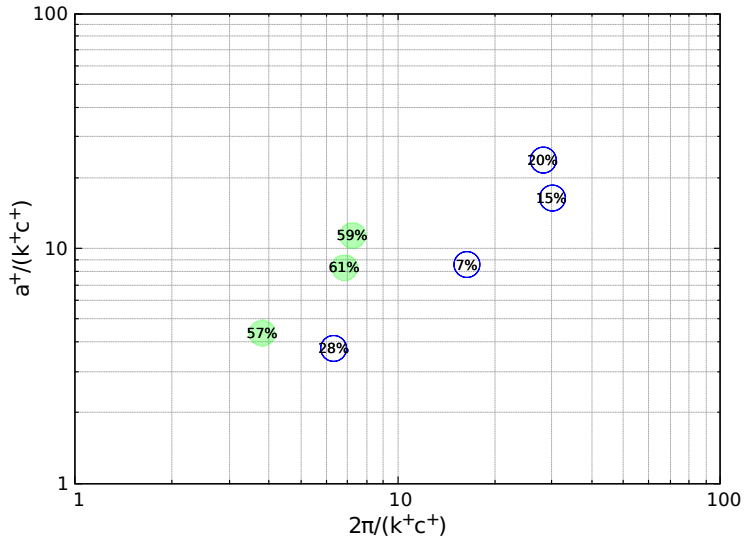

Figure 5.14: *Drag reduction rate map as function of actuation parameters. Green circles, relaminarization cases; blue circles, ordinary drag reduction cases. Numbers represent drag reduction rates* $D_R\%$

the flow, and a contribution due to the peristaltic pumping.

To the purpose of assessing drag reduction perormances of different wall actuation strategies, the drag reduction rate D_R can be defined as done in [20]. Particularly:

$$D_R = \frac{G_{p0} - G_p}{G_{p0}} \tag{5.18}$$

where G_{p0} and G_p are the time-averaged mean pressure gradients for the uncontrolled and controlled flows respectively.

Fig.5.14 represents a map, similar to that reported in [35], that displays the computed drag reduction rates for all cases in terms of the actuation

Case	Relaminarization	$D_R\%$
01	yes	61
02	yes	57
03	yes	59
04	no	15
05	no	7
06	no	28
07	no	20

Table 5.3: *Measured drag reduction rates. Green cells indicate relaminarization cases*

parameters a, k and c expressed in wall units. As explained in [34] in the context of rough walls, viscous units should be based on the friction velocity defined taking into account the total stress at the wall (thus both friction and pressure contributions should be accounted for). The same convention was adopted in the present study.

There is a good qualitative agreement between the drag reduction performances presented in this section with those found in [35]. Stable relaminarization occurred under the same set of actuation parameters reported by Nakanishi *et al.* and large drag reductions were observed with these cases. For all other cases the flow remained turbulent for the entire simulation and weaker drag reductions were measured. However, a direct quantitative comparison of the rates of drag reduction with data reported in [35] reveals a considerable difference. In their work, the drag reduction rate is computed from the actual external pressure gradient used to pump the flow. In the present study, the measured value of the pressure gradient is polluted by the pumping induced by wall actuation; thus it is the sum of two contributions: one comes from the external pressure jump (enforced to drive the flow), the other is the peristaltic pumping contribution (induced by wall motion).

Chapter 6

Conclusions

In the present study, an existing flow-solver for the simulation of turbulent channel flow over stationary rough walls has been adapted to simulate the presence of non-planar moving solid boundaries. Specifically, only a wall-normal motion of the walls has been considered. The method performs a spatial discretization on a fixed, non-body-conformal, Cartesian grid using second-order accurate finite differences. Time advancement is realized using a fractional-step technique and employing a three-step Runge-Kutta method. No-slip boundary conditions on the solid boundary of the channel are enforced through a direct correction to the discrete momentum equation without resorting to any complex interpolation procedure.

The described numerical method has been employed for the simulation of turbulent flow through a peristaltic actuator. The latter consists of a channel of indefinite extension (in the streamwise and spanwise directions) controlled via streamwise traveling waves of wall deformation. In particular, the channel surfaces deform only in-phase along the streamwise direction with a prescribed sinusoidal law.

The Reynolds number (based on the mean bulk velocity) for all the simulations was Re_b = 2800, corresponding to a friction Reynolds number Re_τ = 180 for the uncontrolled channel (*i.e.* plane channel). The results obtained are in good agreement with those of Nakanishi *et al.* in [35]. In their study the peristaltic actuation leads to drag reduction for all the waves traveling downstream at a phase-speed exceeding the speed of the mean flow. Moreover, for some sets of parameters, they report a full relaminarization of the flow. The same qualitative behavior has been observed in the present study; for cases 01, 02 and 03 (corresponding to relaminarization cases 8, 9 and 11 of Nakanishi *et al.*) a stable relaminarization of the flow occurred.

For all other cases studied in the present work, the flow has been observed to remain turbulent for the entire simulation. However, measures of the mean pressure gradient used to drive the flow at a constant rate show that drag reduction is achieved with respect to the uncontrolled reference

case. Unfortunately a direct quantitative comparison of the drag reduction rates with data reported by Nakanishi *et al.* reveals a considerable disagreement. In their study the drag reduction rate is computed from the actual external mean pressure gradient enforced to drive the flow through the channel. Conversely, in the present study the mean pressure gradient used to compute the drag reduction rate is made up of two contributions: the first is due to the external pumping force used to drive the flow; the second is a sub-product of wall actuation and is termed as peristaltic pumping. The disagreement between the computed drag reduction rates might be addressed to the polluting presence of the peristaltic pumping on the measure of the mean pressure gradient.

Based on the current definition of the drag reduction rate, the peristaltic actuator has been proved to be highly effective in weakening turbulence and leading to drag reduction rates up to 61% for relaminarization *case* 01 and up to 28% for the fully turbulent *case* 06.

Motivated by these findings, a further intensive parametric study of the peristaltic actuator would be of great interest. It is not clear indeed what is the effect of each actuation parameter on drag reduction performances and the relaminarization phenomenon. Moreover, a future investigation should be aimed at assessing the Reynolds number dependence; relaminarization occurred easily in the cases tested in this study because of the relatively low Reynolds number considered. However, it is natural to expect that the destabilizing effect of turbulence may eventually overcome the stabilizing effect of the traveling waves as the Reynolds number increases. Up to what Reynolds number relaminarization occurs is then a question of significant importance.

Finally, a future implementation of the numerical method, allowing for more complex and arbitrary wall motions, would lead to an entirely new set of research scenarios. Along with this, it comes the necessity of finding an appropriate way for enforcing volume conservation without any restriction on the time-step size/grid spacing, like that adopted in the present work.

Bibliography

[1] T. Bewley. A fundamental limit on the balance of power in a transpiration-controlled channel flow. *Jou. of Fluid Mechanics*, 632:443–446, 2009.

[2] T. Bewley and O. Aamo. A 'win–win' mechanism for low-drag transients in controlled two-dimensional channel flow and its implications for sustained drag reduction. *Jou. of Fluid Mechanics*, 499:183–196, 2004.

[3] P. W. Carpenter and P. J. Morris. The effect of anisotropic wall compliance on boundary-layer stability and transition. *Journal of Fluid Mechanics*, 218, 1990.

[4] P. Cherukat, Y. Na, and T. Hanratty. Direct numerical simulation of a fully developed turbulent flow over a wavy wall. *Theoret. Comput. Fluid Dynamics*, 11:109–134, 1998.

[5] P. A. Davidson. *Turbulence: An Introduction for Scientists and Engineers*. Oxford University Press, USA, 2004.

[6] M. V. Dyke. *An Album of Fluid Motion*. Parabolic Press, Inc., 12th edition, 2008.

[7] T. Endo and R. Himeno. Direct numerical simulation of turbulent flow over a compliant surface. *Journal of Turbulence*, 3, 01 2002.

[8] K. Fukagata. Drag reduction by wavy surfaces. *Jou. of Fluid Science and Technology*, 6:2–13, 2011.

[9] K. Fukagata, K. Iwamoto, and N. Kasagi. Contribution of reynolds stress distribution to the skin friction in wall-bounded flows. *Physics of Fluids*, 14:L73–L76, 2002.

[10] K. Fukagata, K. Iwamoto, and N. Kasagi. Contribution of reynolds stress distribution to the skin friction in wall-bounded flows. *Physics of Fluids*, pages 73–76, 2002.

[11] K. Fukagata, S. Kern, P. Chatelain, P. Koumoutsakos, and N. Kasagi. Evolutionary optimization of an anisotropic compliant surface for turbulent friction drag reduction. *Journal of Turbulence*, 9, 2008.

[12] K. Fukagata, K. Sugiyama, and N. Kasagi. On the lower bound of net driving power in controlled duct flows. *Physica*, 238:1082–1086, 2009.

[13] P. Garrad, A.D.and Carpenter. A theoretical investigation of flow-induced instabilities in compliant coatings. *Journal of Sound and Vibration*, 85:483–500, 1982.

[14] J. L. L. H. Tennekes. *A first course in turbulence*. MIT Press, 1972.

[15] Y. Hasegawa, M. Quadrio, and F. B. Numerical simulation of turbulent duct flows at constant power input. *Jou. of Fluid Mech.*, 750:191–209, 2014.

[16] J. Hoepffner and K. Fukagata. Pumping or drag reduction? *Jou. of Fluid Mechanics*, 635:171–187, 2009.

[17] J. Hudson, L. Dykhno, and T. Hanratty. Turbulence production in a flow over a wavy wall. *Experiments in Fluids*, 20:257–265, 1996.

[18] G. Iaccarino and R. Verzicco. Immersed boundary technique for turbulent flow simulations. *Appl. Mech. Reviews*, 56:331–347, 2003.

[19] S. Kang and H. Choi. Active wall motions for skin-friction drag reduction. *Physics of Fluids*, 12:3301–3304, 2000.

[20] N. Kasagi, Y. Hasegawa, and F. K. Toward cost-effective control of wall turbulence for skin friction drag reduction. *Advances in Turbulence XII, Springer Proceedings in Physics*, 132:189–200, 2009.

[21] J. Kim, D. Kim, and H. Choi. An immersed-boundary finite-volume method for simulations of flow in complex geometries. *Jou. of Comp. Physics*, 171:132–150, 2001.

[22] J. Kim, P. Moin, and R. Moser. Turbulence statistics in fully developed channel flow at low reynolds number. *Jou. of Fluid Mechanics*, 177:133–166, 1987.

[23] C. Lee, T. Min, and J. Kim. Stability of a channel flow subject to wall blowing and suction in the form of a traveling wave. *Physics of Fluids*, 20:101513, 2008.

[24] J. Lee, J. Kim, H. Choi, and K. Yang. Sources of spurious force oscillations from an immersed boundary method for moving-body problems. *Jou. of Comp. Physics*, 230:2677–2695, 2011.

[25] B. K. Lieu, R. Moarref, and M. R. Jovanovic. Controlling the onset of turbulence by streamwise travelling waves. part 2. direct numerical simulation. *Journal of Fluid Mechanics*, 663:100–119, 2010.

[26] P. Luchini. Immersed-boundary simulations of turbulent flow past a sinusoidally undulated river bottom. *Europ. Jou. of Mech. B/Fluids*, 55:340–347, 2016.

[27] H. Luo and T. Bewley. Accurate simulation of near-wall turbulence over a compliant tensegrity fabric. *SPIE Smart Structures and Materials*, 5757, 2005.

[28] H. Luo, H. Dai, P. Ferreira de Sousa, and B. Yin. On the numerical oscillation of the direct-forcing immersed-boundary method for moving boundaries. *Computer and Fluids*, 56:61–76, 2012.

[29] H. Mamori, K. Fukagata, and J. Hoepffner. Phase relationship in laminar channel flow controlled by traveling-wave-like blowing or suction. *Physical Review E*, 81:046304, 2010.

[30] H. Mamori, K. Iwamoto, and A. Murata. Effect of the parameters of traveling waves created by blowing and suction on the relaminarization phenomena in fully developed turbulent channel flow. *Physics of Fluids*, 26, 2014.

[31] T. Min, S. Kang, J. Speyer, and J. Kim. Sustained sub-laminar drag in a fully developed channel flow. *Jou. of Fluid Mechanics*, 558:309–318, 2006.

[32] R. Mittal and G. Iaccarino. Immersed boundary methods. *Ann. Review of Fluid Mech.*, 37:239–261, 2005.

[33] R. Moarref and M. R. Jovanovic. Controlling the onset of turbulence by streamwise travelling waves. part 1. receptivity analysis. *Journal of Fluid Mechanics*, 663:70–99, 2010.

[34] E. Mori, M. Quadrio, and K. Fukagata. Turbulent drag reduction by uniform blowing over a two-dimensional roughness. *Flow, Turbulence and Combustion*, 99:765–785, 2017.

[35] R. Nakanishi, H. Mamori, and K. Fukagata. Relaminarization of turbulent channel flow using traveling wave-like wall deformation. *Int. Jou. of Heat and Fluid Flow*, 35:152–159, 2012.

[36] S. V. Patankar. *Numerical heat transfer and fluid flow.* McGraw-Hill Inc., New York, US, 1 edition, 1980.

[37] C. Peskin. Flow patterns around heart valves: a numerical method. *Jou. of Comp. Physics*, 10:252–271, 1972.

[38] C. Peskin. The immersed boundary method. *Acta Numerica*, pages 479–517, 2002.

[39] S. B. Pope. *Turbulent flows*. Cambridge University Press, 1 edition, 2000.

[40] A. Prosperetti and G. Tryggvason. *Computational methods for multiphase flow*. Cambridge University Press, 2009.

[41] M. Quadrio, B. Frohnapfel, and Y. Hasegawa. Does the choice of the forcing term affect flow statistics in DNS of turbulent channel flow? *European Jou. of Mech. B/Fluids*, 56:286–293, 2016.

[42] O. Reynolds. An experimental investigation of the circumstances which determine whether the motion of water shall be direct or sinuous, and of the law of resistance in parallel channels. *Philosophical Transactions of the Royal Society of London*, 174:935–982, 1883.

[43] W. Reynolds and A. K. M. F. Hussain. The mechanics of an organized wave in turbulent shear flow. *Jou. of Fluid Mechanics*, 41:241–258, 1970.

[44] S. Robinson. Coherent motions in the turbulent boundary layer. *Ann. Review of Fluid Mech.*, 23:601–639, 1991.

[45] W. Schoppa and F. Hussain. Coherent structure dynamics in near-wall turbulence. *Fluid Dynamics Research*, 26:119–139, 2000.

[46] J. Seo and R. Mittal. A sharp-interface immersed boundary method with improved mass conservation and reduced spurious pressure oscillations. *Jou. of Comp. Physics*, 230:7347–7363, 2011.

[47] L. Shen, X. Zhang, D. Yue, and M. Triantafyllou. Turbulent flow over a flexible wall undergoing a streamwise travelling wave motion. *Jou. of Fluid Mechanics*, 484:197–221, 2003.

[48] S. Taneda and Y. Tomonari. An experiment on the flow around a waving plate. *Journal of the Physical Society of Japan*, 36:1683–1689, 1974.

[49] Y. Tseng and J. Ferziger. A ghost-cell immersed boundary method for flow in complex geometry. *Jou. of Comp. Physics*, 192:593–623, 2003.

[50] H. Udaykumar, R. Mittal, P. Rampunggoon, and A. Khanna. A sharp interface cartesian grid method for simulating flows with complex moving boundaries. *Jou. of Comp. Physics*, 174:345–380, 2001.

[51] P. Viswanath. Aircraft viscous drag reduction using riblets. *Progress in Aerospace Sciences*, 38:571–600, 2002.

[52] T. Ye, R. Mittal, H. Udaykumar, and W. Shyy. An accurate cartesian grid method for viscous incompressible flows with complex immersed boundaries. *Jou. of Comp. Physics*, 156:209–240, 1999.